

Performance Analysis of In-Band-Full-Duplex Multi-Cell Wideband IAB Networks

Junkai Zhang, *Student Member, IEEE*, and Tharmalingam Ratnarajah, *Senior Member, IEEE*

Abstract—This paper analyzes the performance of the 3rd Generation Partnership Project (3GPP)-inspired multi-cell wideband single-hop backhaul millimeter-wave-in-band-full-duplex (IBFD)-integrated access and backhaul (IAB) networks by using stochastic geometry. We model the wired-connected Next Generation NodeBs (gNBs) as the Matérn hard-core point process (MHCPP) to meet the real-world deployment requirement and reduce the cost caused by wired connection in the network. We first derive association probabilities that reflect how likely the typical user-equipment is served by a gNB or an IAB-node based on the maximum long-term averaged biased-received-desired-signal power criteria. Further, by leveraging the composite Gamma-Lognormal distribution, we derive the closed-form signal to interference plus noise ratio coverage, capacity with outage, and ergodic capacity of the network. In order to avoid underestimating the noise, we consider the sidelobe gain on inter-cell interference links and the analog to digital converter quantization noise. Compared with the half-duplex transmission, numerical results show an enhanced capacity with outage and ergodic capacity provided by IBFD under successful self-interference cancellation. We also study how the power bias and density ratio of the IAB-node to gNB, and the hard-core distance can affect system performances.

Index Terms—Millimeter-wave, integrated access and backhaul, in-band-full-duplex, Matérn hard-core point process, stochastic geometry.

I. INTRODUCTION

MILLIMETER-wave (mmWave) communications have been provided to satisfy the urgent demand for large available bandwidth in the beyond fifth-generation (5G) communications, as the number of wireless devices increases sharply in current networks [1], [2]. Although the large available bandwidth among 30-300 GHz can significantly increase the capacity of the wireless network, the path loss becomes more severe than that in microwave communications due to the effective antenna aperture being proportional to the wavelength. Therefore, dense base station (BS) deployment with large-scale antenna arrays is required. For hardware and power efficiency, fully-connected/subarray hybrid beamforming is used for mmWave communications [3], [4].

To further explore the benefit of the mmWave spectrum, the in-band-full-duplex (IBFD) transmission, where transmission and reception occur at the same time and frequency band, is proposed [5]. Compared with the half-duplex (HD) transmission, the IBFD scheme provides twice the spectral efficiency (SE) and half the latency [6]. However, dealing with the self-interference (SI), which can be more than 100 dB higher than

the desired signal, becomes the biggest challenge in realizing the IBFD transmission. Fortunately, a combination of antenna [7], analog [6], and digital [8] SI cancellation (SIC) can achieve satisfactory performance in mmWave IBFD networks.

Moreover, integrated access and backhaul (IAB) networks have been studied in the technical specifications—TR 38.874 (Rel. 16) provided by the 3rd Generation Partnership Project (3GPP) [9], where wireless backhaul is introduced instead of fiber connections. Plug-and-play deployment [9], multi-hop networks [10], and performance analysis [11] in IAB networks have been involved in recent research topics. Although authors in [12] concludes that all-wired networks (i.e., all BSs connect to the core network by fiber directly) give better performance than IAB networks, IAB networks provide a good solution for reducing the deployment cost in mmWave communications. Even if we designed single-cell wideband single-hop backhaul mmWave-IBFD-IAB networks in [1], [8], more profound studies on the performance analysis of multi-cell wideband single-hop backhaul mmWave-IBFD-IAB networks are lacking in the literature, which becomes the main subject of this work.

In prior works [2], [11], [13], [14], stochastic geometry is used to analyze the performance of IAB networks. However, none of these works considers the IBFD transmission and hybrid beamforming except for [2]. In addition, in terms of the distribution of small fading, only [11] considers the Nakagami- M distribution, which is more suitable for mmWave communications than using the Rayleigh distribution since the Rayleigh fading model for sub-6 GHz communications is predicated on a large amount of local scattering, which is not the case for mmWave communications [15]. Moreover, the shadowing effect is lacking in most of these works. Only [14] considers both small fading and path loss with the shadowing effect; however, the Rayleigh distribution is used for modeling the small fading rather than the Nakagami- M distribution. Therefore, to analyze a more general mmWave-IAB network suitable for beyond 5G communications, we consider the IBFD, hybrid beamforming, Nakagami- M small fading, and Lognormal shadowing effect in this work.

In the real world, the BSs are not entirely deployed randomly or regularly, which results in the deterministic or Poisson point process (PPP) model becoming insufficient. Therefore, non-Poisson models are preferred for modeling real-world BS deployment. For analytical tractability, authors in [16] suggested a method that uses PPP to approximate the signal-to-interference ratio meta-distribution for non-Poisson networks, which can provide good accuracy. In this work, to model the deployment of the wired-connected Next Generation NodeBs (gNBs), i.e., the IAB donors, the Matérn hard-core

J. Zhang, and T. Ratnarajah are with Institute for Digital Communications, The University of Edinburgh, Edinburgh, EH9 3FG, UK (e-mail: {jzhang15, T. Ratnarajah}@ed.ac.uk).

point process (MHCPP) is applied, where a hard-core distance (i.e., the minimum distance that two gNBs are separated in the network). The MHCPP model reflects the repulsion among gNBs since gNBs act as wired-anchored BSs. Two gNBs should not be too close or overlap. Moreover, while providing satisfactory service quality, MHCPP generates less density of gNBs than PPP, which avoids the high cost due to the wired connection. Although MHCPP has been applied for modeling unmanned aerial vehicles [17], multi-cell IBFD cellular networks [18], and cloud radio access networks [19], to our best knowledge, we are the first who introduce MHCPP into the analysis of multi-cell mmWave-IBFD-IAB networks.

In this paper, we evaluate the performance of the multi-cell wideband single-hop backhaul mmWave-IBFD-IAB networks using stochastic geometry. Our main contributions are summarized below.

- Unlike previous studies on mmWave communications using stochastic geometry, which do not consider hybrid beamforming, we analyze the performance with energy-efficient subarray-based hybrid beamforming since mmWave communications need to adopt large-scale antenna arrays. The use of hybrid beamforming has less hardware cost and power consumption than transitional full digital beamforming. Unlike prior works on IAB networks, which use PPP to model the location of gNBs, we use MHCPP to meet the real-world deployment scenario that BSs are deployed likely in the non-Poisson model. In this way, the wired-connected gNBs, acting as anchored BSs, can be deployed without overlapping or being too close. Additionally, MHCPP produces fewer gNBs than PPP, which reduces the cost of deploying wired gNBs. We use the probability generating functional (PGFL) of PPP to estimate the mean interference from gNBs in the backhaul link and gNB associated access link, which makes the analysis more tractable.
- Instead of analyzing the performance of mmWave-HD-all-wired networks, we consider mmWave-IBFD-IAB networks, which satisfy the requirement of enhanced communication performance and dense deployment with less cost in beyond 5G communications. The IAB-nodes are operating in IBFD mode for simultaneous transmission and reception. Assuming successful SIC, only residual SI (RSI), modeled as Gaussian noise, is considered whose power is a fraction of the transmit power.
- To accurately model the channel and path loss for mmWave communications, we consider the Nakagami- M small fading and include Lognormal shadowing effect in the path loss model, which is different from most existing literature on mmWave communications using stochastic geometry. For tractability, we introduce the closed-form statistical property of the composite Gamma-Lognormal (GL) distribution to derive the analytical results.
- To avoid the underestimation of noise and interference, we consider the sidelobe gain for the inter-cell interference links and the analog to digital converter (ADC) quantization noise.

Numerical results show that by tuning the bias ratio of

the IAB-node to gNB, the signal to interference plus noise ratio (SINR) coverage gives a convex-alike curve at a fixed SINR threshold. With a selected bias ratio (e.g., 0 dB), the capacity with outage of the IBFD scheme outperforms that of the HD scheme, regardless of the RSI power. In addition, for our default simulation setting, at SINR = 0 dB, the ADC quantization noise effect becomes negligible at around 5 bits resolution, which emphasizes the feasibility of using low-resolution ADC in our proposed network. Moreover, under the same gNB density, the network ergodic capacity given by deploying gNBs with PPP-based model is less than that given by deploying gNBs with MHCPP-based model; the larger the hard-core distance, the higher the ergodic capacity. In addition, with successful SIC, the ergodic capacity increases as the density ratio of IAB-node to gNB increases.

Notations: $\mathcal{B}, \mathbf{B}, \mathbf{b}, b$ represent a set, a matrix, a vector, and a scalar, respectively. $\mathbf{B}^H, \mathbf{B}^{-1}$, and \mathbf{B}^T are the Hermitian, inverse, and transpose of \mathbf{B} , respectively. $\text{blkdiag}[\mathbf{B}_1, \mathbf{B}_2]$ is the block diagonal matrix formed by matrix \mathbf{B}_1 and \mathbf{B}_2 . $\|\cdot\|_F$ denotes the Frobenius norm. $|b|$ is the norm of b . $\|\mathbf{b}\|$ is the norm of \mathbf{b} . C_n^k is the possible combinations of k elements out of a group of n elements where order does not matter. $\mathcal{N}(m, n)$ represents normal distribution with mean m and variance n . $\ln\mathcal{N}(m, n)$ denotes Lognormal distribution with parameters m and n . $\mathcal{U}[a, b]$ represents uniform distribution between a and b . $\delta(\cdot)$ is the Dirac delta function.

II. SYSTEM MODEL

A. IAB Network Topology

We consider the downlink of the standalone single-hop backhaul IAB network with spanning tree (ST) topology, which consists of the following nodes,

- IAB donor: it is also called as gNB, which is a single logical node. The gNB connects to the 5G next-generation core network by fiber and wirelessly transmits signals to other types of nodes in the network.
- IAB-node: it operates in the IBFD manner and contributes SI from its transmitter to its receiver and uses wireless links to communicate with others. Due to the single-hop backhaul and ST topology, an IAB-node only has one parent gNB for backhauling.
- User-equipment (UE): it receives desired signal from its serving gNB or IAB-node.

The backhaul link is the wireless link between the gNB and the IAB-node, while the access link is that between the UE and the gNB or the IAB-node. More details on 3GPP architecture can be found in our recent work [1]. An illustration of our system model is depicted in Fig 1(a). In this work, gNBs and IAB-nodes form two different tiers. Multi-hop backhaul IAB networks will not be considered due to the challenge of network configuration, and the feasibility of using stochastic geometry under this scenario [13].

B. Spatial Arrangement

MHCPP has two types, all generated by thinning a parent PPP. In type I, a point and its neighbors whose distance is

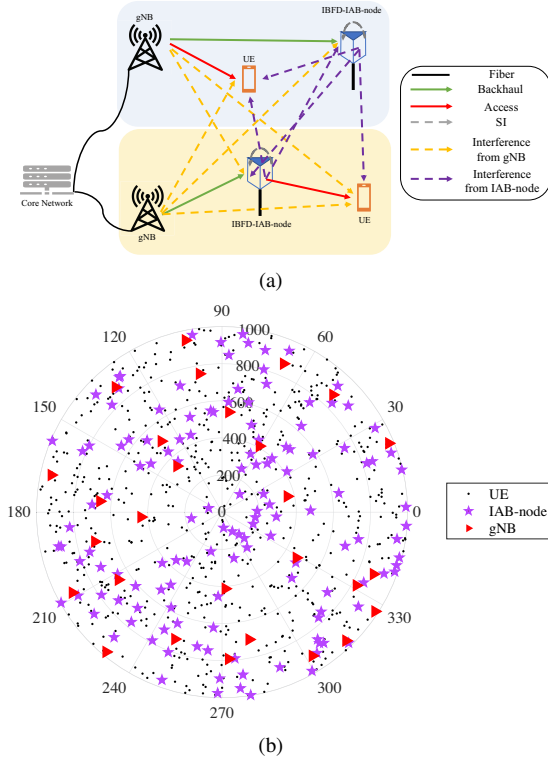


Fig. 1. (a) Illustration of a multi-cell single-hop backhaul mmWave-IBFD-IAB network. (b) A realized mmWave-IBFD-IAB network. $R_0 = 1000\text{m}$, $\lambda_m = 1 \times 10^{-5}/\text{m}^2$, $\lambda_s = 4 \times 10^{-5}/\text{m}^2$, $\lambda_u = 2 \times 10^{-4}/\text{m}^2$, $\xi = 100\text{m}$.

less than the hard-core distance are removed from the parent PPP. In type II, each point is assigned to a random number between 0 and 1 as their marks; only points that have bigger marks and are within the hard-core region of their neighbors are removed [20]. In this work, we utilize MHCPP Type II¹ to capture the location of gNBs. Consider that gNBs are distributed according to an MHCPP Φ_m with density λ_m and hard-core distance ξ on \mathbb{R}^2 , where the density is defined by dependent thinning of a parent homogeneous PPP $\tilde{\Phi}_m$ with density of $\tilde{\lambda}_m$. Given the probability of an arbitrary point in the parent PPP is retained for the MHCPP Type II as

$$\rho = \frac{1 - e^{-\pi\xi^2\tilde{\lambda}_m}}{\pi\xi^2\tilde{\lambda}_m}, \quad (1)$$

we have $\lambda_m = \rho\tilde{\lambda}_m$ [21]. The IAB-nodes and UEs are drawn from two independent homogeneous PPPs Φ_s and Φ_u with density λ_s and λ_u on \mathbb{R}^2 , respectively. Our analysis is done on a circular region with radius R_0 . A realized network is depicted in Fig. 1(b).

C. Propagation Model

1) *Blockage Model*: Since in mmWave frequencies, the signals are easily blocked by obstacles in the propagation environment, which results in the coexistence of line-of-sight (LoS) and non-line-of-sight (NLoS) propagation. The

¹Under the same parent PPP density, the thinning rule of the MHCPP type II is more relaxed than that of the MHCPP Type I, which can give a higher density of gNB to satisfy the dense deployment condition for mmWave communications.

blockages typically form a process of random shapes, e.g., a Boolean scheme of rectangles [22]. In this work, the probability of being LoS $p_L(r)$ or NLoS $p_N(r)$ transmission is modeled by a two-state exponential blockage model with respect to the blockage density constant ϵ and the link distance r [23], which is cast as

$$\begin{cases} p_L(r) = e^{-\epsilon r}, \\ p_N(r) = 1 - e^{-\epsilon r}. \end{cases} \quad (2)$$

Note that we adopt the above model for IAB-nodes since gNBs can have considerable height due to the role of anchored BSs and are usually placed on open ground with fewer obstacles, for tractability, we assume LoS transmission only for gNB to ease the lack of transformation properties of the MHCPP. Moreover, we consider independent blockage effects between links in this work.

Given the blockage model, we can treat the PPP IAB-nodes Φ_s as the superposition of PPP LoS IAB-nodes $\Phi_{s,L}$ and PPP NLoS IAB-nodes $\Phi_{s,N}$ with densities of $\lambda_{s,L}(r) = \lambda_s p_L(r)$ and $\lambda_{s,N}(r) = \lambda_s p_N(r)$, respectively.

2) *Path Loss Model*: The path loss model utilized in [14] is adopted in this work to measure the path loss between two nodes located at \mathbf{x} and \mathbf{y} . The gain for a single antenna element is given as

$$L(\mathbf{x}, \mathbf{y})[\text{dB}] = \beta + 10\alpha \log_{10} R_{\mathbf{xy}} + \chi, \quad (3)$$

where $\beta = 20 \log_{10} \left(\frac{4\pi f_c}{c} \right)$. f_c , c , α , and $\chi \sim \mathcal{N}(0, \zeta^2)$ denote the carrier frequency, light speed, path loss exponent, and shadowing effect random variable, respectively. $R_{\mathbf{xy}}$ represents the Euclidean distance between \mathbf{x} and \mathbf{y} . Therefore, we have $L(\mathbf{x}, \mathbf{y}) = \frac{R_{\mathbf{xy}}^\alpha}{10^{-0.1(\beta+\chi)}}$, where $10^{-0.1(\beta+\chi)} \sim \text{lnN} \left(-0.1\beta \ln 10, (0.1\zeta \ln 10)^2 \right)$ is a Lognormal distributed random variable². Note that the path loss exponent and Gaussian distributed shadowing effect random variable for the transmissions from gNB are denoted as α_m and $\chi_m \sim \mathcal{N}(0, \zeta_m^2)$, respectively. As for the IAB-node, we have the path loss exponent $\alpha_{s,i}$ and shadowing effect random variable $\chi_{s,i} \sim \mathcal{N}(0, \zeta_{s,i}^2)$, where $i = L$ for LoS IAB-node and $i = N$ for NLoS IAB-node.

3) *Channel Model*: Assume an OFDM single-path (i.e., flat fading) channel for all blockage scenarios, which leverages the sparsity of the FR2 band channel. The multi-path case will be left as future. At subcarrier $k = 1, 2, \dots, K$, the wideband mmWave channel from the node at \mathbf{x} with N_T transmit antennas to the node at \mathbf{y} with N_R receive antennas is given as [3]

$$\mathbf{H}_{\mathbf{yx}}[k] = \sqrt{\frac{N_T N_R}{L(\mathbf{x}, \mathbf{y})}} h^{\mathbf{yx}} \gamma[k] \mathbf{a}_R(\bar{\theta}_R^{\mathbf{yx}}, \bar{\phi}_R^{\mathbf{yx}}) \mathbf{a}_T^H(\bar{\theta}_T^{\mathbf{yx}}, \bar{\phi}_T^{\mathbf{yx}}), \quad (4)$$

where $h^{\mathbf{yx}}$ is the small fading gain with Nakagami- M distribution [24]. $M \in \{M_m, M_{s,L}, M_{s,N}\} \in \mathbb{N}^+$ are Nakagami parameters for the gNB, LoS IAB-node, and NLoS IAB-node, respectively. $\gamma[k] = \sum_{d=0}^{D-1} p(d - \tilde{\tau}) e^{-j \frac{2\pi k d}{K}}$ with $p(\cdot)$ being the raised-cosine pulse shaping filter, $\tilde{\tau} \sim \mathcal{U}[0, D]$ being the

²If Z is a normal distributed random variable with zero mean and variance σ^2 , then $X = e^{m+nZ}$ is a Lognormal random variable with parameters $\hat{\mu} = m$ and $\hat{\sigma} = n\sigma$, denoted as $X \sim \text{lnN}(\hat{\mu}, \hat{\sigma}^2)$ with $\mathbb{E}\{X\} = e^{\hat{\mu} + 0.5\hat{\sigma}^2}$.

normalized path delay, and D denoting the number of delay taps.

For simplicity, we leverage the virtual transmit and receive steering vectors $\mathbf{a}_T(\bar{\theta}_T^{yx}, \bar{\phi}_T^{yx})$ and $\mathbf{a}_R(\bar{\theta}_R^{yx}, \bar{\phi}_R^{yx})$ for the uniform planar array (UPA), respectively, where the azimuth $\bar{\theta}_T^{yx}/\bar{\theta}_R^{yx}$ and elevation $\bar{\phi}_T^{yx}/\bar{\phi}_R^{yx}$ virtual angles correspond to the angle of departure/arrival (AoD/AoA) [25]. With half-wavelength spaced elements, we have the relationship between the virtual and physical azimuth (elevation) AoD/AoA as $\bar{\theta} = \pi \cos \theta \cos \phi$ ($\bar{\phi} = \pi \sin \theta \cos \phi$), where $\theta \sim \mathcal{U}[0, \pi]$ and $\phi \sim \mathcal{U}[-\frac{\pi}{2}, \frac{\pi}{2}]$ are the physical azimuth and elevation AoD/AoA. By extending the model in [25], we have the virtual azimuth and elevation AoD/AoA are quantized to sets $\bar{\theta} \in \{-\frac{\pi}{2}, -\frac{\pi}{2} + \frac{\pi}{N_x}, \dots, -\frac{\pi}{2} + \frac{\pi(N_x-1)}{N_x}\}$ and $\bar{\phi} \in \{0, \frac{\pi}{N_y}, \dots, \frac{\pi(N_y-1)}{N_y}\}$ with N_x and N_y being the number of antennas along x - and y -axis of the UPA. Moreover, we assume the virtual angles are uniformly distributed in their quantized sets for tractability [26]. From the orthogonality of the virtual steering vector, we have $\mathbf{a}^H(\bar{\theta}_1, \bar{\phi}_1)\mathbf{a}(\bar{\theta}_2, \bar{\phi}_2) = 1$ for $\bar{\theta}_1 = \bar{\theta}_2, \bar{\phi}_1 = \bar{\phi}_2$ and 0 otherwise [27, Corollary 2], which gives us an ON/OFF model. With this ON/OFF model, the SINR expressions can be simplified.

Since this work aims to evaluate the performance of the IBFD-IAB networks after the SI has been successfully suppressed, only the residual SI, treated as Gaussian noise, whose power is modeled as a fraction of transmit power, will be considered. Readers are directed to [8] for a hypothetical Rician-alike SI channel model and staged SIC strategy.

III. ANTENNA CONFIGURATION AND BEAMFORMING DESIGN

A. Antenna Configuration

The gNB and IAB-node transmitters are adopted with subarray-based hybrid beamforming (i.e., one RF chain connects with only a portion of antennas), as proposed in [3], [8]. The gNB has N_m subarrays; each has $\frac{N_T}{N_m}$ transmit antennas and one RF chain sending single data stream for serving one UE or IAB-node. Similarly, the IAB-node is equipped with N_s subarrays; each has $\frac{N_T}{N_s}$ transmit antennas and a single RF chain sending one data stream to serve a UE. The IAB-node receiver is equipped with N_R^s receive antennas adopting analog combining for receiving information from its serving gNB. The UE receiver has N_R^u antennas with analog combining for communicating with its serving BS.

B. Beamforming Design

According to the subarray hybrid beamforming structure given in [3], the RF and BB precoders at gNBs and IAB-nodes have the form of $\mathbf{F}_{\text{RF}}^{(\cdot)} = \text{blkdiag}[\mathbf{f}_{\text{RF},1}^{(\cdot)}, \mathbf{f}_{\text{RF},2}^{(\cdot)}, \dots, \mathbf{f}_{\text{RF},N_i}^{(\cdot)}] \in \mathbb{C}^{N_T \times N_i}$ and $\mathbf{F}_{\text{BB}}^{(\cdot)}[k] = [\mathbf{f}_{\text{BB},1}^{(\cdot)}[k], \mathbf{f}_{\text{BB},2}^{(\cdot)}[k], \dots, \mathbf{f}_{\text{BB},N_i}^{(\cdot)}[k]] \in \mathbb{C}^{N_i \times N_i}$, respectively, where (\cdot) is the location of the gNB or IAB-node; $i = m$ represents the precoders at the gNB and $i = s$ is those at the IAB-node. The RF combiner at the IAB-node and UE are in the form of $\mathbf{w}_{\text{RF}}^{(\cdot)} \in \mathbb{C}^{N_R^i \times 1}$, where $i = s$ denotes the combiner at the IAB-node and $i = u$ is that at the UE.

The RF beamformers are realized by phase shifters (PSs) with unit norm entries. According to [26], the optimal RF precoder/combiner that maximizes the desired signal power is to steer the beam in the direction of the AoD/AoA of the desired signal channel. Given the channel from the transmitter at \mathbf{x} to the receiver at \mathbf{y} in (4), due to the use of subarray-based hybrid beamforming, a subset of the virtual transmit steering vector is used to design the v th column of the RF precoder matrix \mathbf{F}_{RF}^x , that is

$$\mathbf{f}_{\text{RF},v}^x = \sqrt{N_T^i} [\mathbf{a}_T(\bar{\theta}_T^{yx}, \bar{\phi}_T^{yx})]_{(v-1)\frac{N_T^i}{N_i} + (1:\frac{N_T^i}{N_i})}, \quad (5)$$

where $i = m$ represents the RF precoder at the gNB and $i = s$ denotes that at the IAB-node.

Similarly, the RF combiner is given by the virtual receive steering vector, that is

$$\mathbf{w}_{\text{RF}}^y = \sqrt{N_R^i} \mathbf{a}_R(\bar{\theta}_R^{yx}, \bar{\phi}_R^{yx}), \quad (6)$$

where $i = s$ denotes the combiner at the IAB-node and $i = u$ is that at the UE.

In order to mitigate the intra-cell interference, the zero-forcing (ZF) BB precoder is utilized both at the gNB and IAB-node. For a transmitter at \mathbf{x} , given its all serving receivers at $\mathbf{y}_1, \mathbf{y}_2, \dots, \mathbf{y}_{N_i}$ (for $i = m$ if \mathbf{x} is a gNB and $i = s$ if \mathbf{x} is an IAB-node), the ZF BB precoder matrix can be given as

$$\mathbf{F}_{\text{BB}}^x[k] = \tilde{\mathbf{H}}_{\text{yx}}^H[k] \left(\tilde{\mathbf{H}}_{\text{yx}}[k] \tilde{\mathbf{H}}_{\text{yx}}^H[k] \right)^{-1}, \quad (7)$$

where $\tilde{\mathbf{H}}_{\text{yx}}[k] = (\mathbf{W}_{\text{RF}}^y)^H \hat{\mathbf{H}}_{\text{yx}}[k] \mathbf{F}_{\text{RF}}^x$ with $\mathbf{W}_{\text{RF}}^y = \text{blkdiag}[\mathbf{w}_{\text{RF}}^{y_1}, \mathbf{w}_{\text{RF}}^{y_2}, \dots, \mathbf{w}_{\text{RF}}^{y_{N_i}}]$ and $\hat{\mathbf{H}}_{\text{yx}}[k] = [\mathbf{H}_{\mathbf{y}_1\mathbf{x}}^T[k], \mathbf{H}_{\mathbf{y}_2\mathbf{x}}^T[k], \dots, \mathbf{H}_{\mathbf{y}_{N_i}\mathbf{x}}^T[k]]^T$.

IV. SINR CHARACTERIZATION

In this section, we derive SINR expressions at the k th subcarrier. According to Slivnyak's theorem [20], given that both IAB-nodes and UEs are homogeneous PPP, we consider typical backhaul and access links without loss of generalization, i.e., we derive the typical backhaul (access) link SINR by assuming the typical IAB-node (UE) located at the origin $\hat{\mathbf{0}}$ ($\mathbf{0}$). Note that $\mathbf{0}$ and $\hat{\mathbf{0}}$ represent the origin in the same coordinate system.

Assume that we know the channel state information perfectly for all channels and that all signals are uncorrelated. Let the average total transmit power at the gNB (IAB-node) across all subcarriers be P_m (P_s). With equal power allocation, each data stream at subcarrier k transmitted from the gNB (IAB-node) has the power of $\frac{P_m}{KN_m}$ ($\frac{P_s}{KN_s}$). Moreover, as the ZF precoder is applied, the intra-cell interference can be canceled out, thus is ignored in the following equations. Besides, a remark is given below for simplifying the analysis.

Remark 1 [2]: The channel model in (4) is the function of k , where k appears only in $\gamma[k]$. Since our work is based on a probabilistic perspective, for tractability, we assume the normalized path delay to be $\tilde{\tau} = \frac{D}{2}$, which is the mean of the random variable $\tilde{\tau}$. Given the channel is flat fading, all subcarriers experience the same channel conditions, thus, we have $\mathbb{E}\{|\gamma[k]|^2\} = 1 \forall k$, which makes the channel independent of k .

1) *Backhaul link*: Assume the gNB at \mathbf{x}_m uses its v th subarray to provide the backhaul communication with the typical IAB-node at $\hat{\mathbf{O}}$, the SINR of the typical backhaul link at the k th subcarrier is written as $\text{SINR}_{\hat{\mathbf{O}}\mathbf{x}_m}[k] =$

$$\frac{G_b[k]}{I_{m,b}[k] + I_{s,b}[k] + \underbrace{\frac{\eta P_s}{K}}_{\text{RSI}} + \mathbb{E}\left\{\left|(\mathbf{w}_{\text{RF}}^{\hat{\mathbf{O}}})^H \mathbf{n}_b[k]\right|^2\right\} + \mathbb{E}\{|e_b[k]|^2\}}, \quad (8a)$$

$$G_b[k] = \frac{P_m}{KN_m} \left| \left(\mathbf{w}_{\text{RF}}^{\hat{\mathbf{O}}} \right)^H \mathbf{H}_{\hat{\mathbf{O}}\mathbf{x}_m}[k] \mathbf{F}_{\text{RF}}^{\mathbf{x}_m} \mathbf{f}_{\text{BB},v}^{\mathbf{x}_m}[k] \right|^2 \\ \approx \frac{P_m N_T^m (N_R^s)^2 \tilde{h}^{\hat{\mathbf{O}}\mathbf{x}_m} p_{\text{ZF}}(N_T^m, N_m)}{KN_m^2 R_{\mathbf{x}_m \hat{\mathbf{O}}}^{\alpha_m}}, \quad (8b)$$

$$I_{m,b}[k] = \frac{P_m}{KN_m} \left\| \sum_{\substack{\omega \in \\ \Phi_m \setminus \mathbf{x}_m}} \left(\mathbf{w}_{\text{RF}}^{\hat{\mathbf{O}}} \right)^H \mathbf{H}_{\hat{\mathbf{O}}\omega}[k] \mathbf{F}_{\text{RF}}^{\omega} \mathbf{F}_{\text{BB}}^{\omega}[k] \right\|^2 \\ \approx \sum_{\substack{\omega \in \\ \Phi_m \setminus \mathbf{x}_m}} \frac{P_m N_T^m (N_R^s)^2 \tilde{h}^{\hat{\mathbf{O}}\omega} p_{\text{BF}}(N_T^m, N_R^s, N_m)}{KN_m R_{\omega \hat{\mathbf{O}}}^{\alpha_m}}, \quad (8c)$$

$$I_{s,b}[k] = \sum_{i \in \{L, N\}} I_{s,b}^i[k] \\ = \frac{P_s}{KN_s} \left\| \sum_{i \in \{L, N\}} \sum_{\hat{\omega} \in \Phi_{s,i} \setminus \hat{\mathbf{O}}} \left(\mathbf{w}_{\text{RF}}^{\hat{\mathbf{O}}} \right)^H \mathbf{H}_{\hat{\mathbf{O}}\hat{\omega}}[k] \mathbf{F}_{\text{RF}}^{\hat{\omega}} \mathbf{F}_{\text{BB}}^{\hat{\omega}}[k] \right\|^2 \\ \approx \sum_{i \in \{L, N\}} \sum_{\hat{\omega} \in \Phi_{s,i} \setminus \hat{\mathbf{O}}} \frac{P_s N_T^s (N_R^s)^2 \tilde{h}^{\hat{\mathbf{O}}\hat{\omega}} p_{\text{BF}}(N_T^s, N_R^s, N_s)}{KN_s R_{\hat{\omega} \hat{\mathbf{O}}}^{\alpha_s}}, \quad (8d)$$

where in (8a), $G_b[k]$, $I_{m,b}[k]$, and $I_{s,b}[k]$ denote the power of the desired signal, that of the interference from non-target gNBs, and that of the interference from IAB-nodes at subcarrier k , respectively; $0 < \eta < 1$ is the RSI controlling factor, which controls the amount of RSI;

$\mathbb{E}\left\{\left|(\mathbf{w}_{\text{RF}}^{\hat{\mathbf{O}}})^H \mathbf{n}_b[k]\right|^2\right\} = \sigma_n^2 N_R^s$ is the Gaussian noise power

with $\mathbf{n}_b[k] \sim \mathcal{CN}(\mathbf{0}, \sigma_n^2 \mathbf{I}_{N_R^s})$; $\mathbb{E}\{|e_b[k]|^2\}$ represents the quantization noise power due to q bits ADC uniform quantization. In (8b)-(8d), $\tilde{h}^{\hat{\mathbf{O}}\mathbf{x}_m} = 10^{-0.1(\beta + \chi_m)} \left| h^{\hat{\mathbf{O}}\mathbf{x}_m} \right|^2$, $\tilde{h}^{\hat{\mathbf{O}}\omega} = 10^{-0.1(\beta + \chi_m)} \left| h^{\hat{\mathbf{O}}\omega} \right|^2$, and $\tilde{h}^{\hat{\mathbf{O}}\hat{\omega}} = 10^{-0.1(\beta + \chi_{s,i})} \left| h^{\hat{\mathbf{O}}\hat{\omega}} \right|^2$ follow

the composite GL distribution (see Appendix-A) since $|h^{(\cdot)}|^2$ is a Gamma distributed random variable³; $p_{\text{ZF}}(N_T^m, N_m)$ is the ZF penalty, which is a Bernoulli random variable with success probability $(1 - \frac{1}{N_T^m})^{N_m - 1}$ (see Remark 2); $p_{\text{BF}}(N_T^m, N_R^s, N_m)$ and $p_{\text{BF}}(N_T^s, N_R^s, N_s)$ are beamforming gains that take into account the sidelobe gains (see Proposition 1) since using the ON/OFF model given by the orthogonality of steering vector can result in underestimating the inter-cell interference as it gives zero beamforming gain when the azimuth and/or elevation angles are not the same. The approximation in (8b) is due to the ZF penalty. The approximation in (8c) is resulted by assuming $\mathbf{F}_{\text{BB}}^{\omega}[k] = \sqrt{\frac{N_T^m}{N_m}} \mathbf{I}_{N_m}$, where $\sqrt{\frac{N_T^m}{N_m}}$ ensures $\|\mathbf{F}_{\text{RF}}^{\omega} \mathbf{F}_{\text{BB}}^{\omega}\|_F^2 = N_m$, since for large number of antennas, the ZF penalty and the effect of ZF on the inter-cell interference

link can be neglected, as evaluated in [4], and (8d) follows the similar approximation.

According to [28], the ADC quantization noise power can be approximated as

$$\mathbb{E}\{|e_b[k]|^2\} \approx \frac{1}{K} \sum_{k'=0}^{K-1} \frac{G_b[k'] + \eta_{\text{dig}} \frac{\eta P_s}{K} + I_{m,b}[k'] + I_{s,b}[k'] + \sigma_n^2 N_R^s}{1.5 \cdot 2^{2q}}, \quad (9)$$

where $\eta_{\text{dig}} > 1$ is the amount of digital cancellation, which is introduced to reproduce the RSI power before ADC (i.e., after analog SIC) since $\frac{\eta P_s}{K}$ is the RSI power after ADC (i.e., after digital SIC). q denotes the ADC quantization bits. Thanks to the Remark 1, the value on the numerator of (9) is the same for all subcarriers, thus, (9) can be simplified as

$$\mathbb{E}\{|e_b[k]|^2\} \approx \frac{G_b[k] + \eta_{\text{dig}} \frac{\eta P_s}{K} + I_{m,b}[k] + I_{s,b}[k] + \sigma_n^2 N_R^s}{1.5 \cdot 2^{2q}} \quad (10)$$

Remark 2 [26]: For notation simplicity, we assume the transmitter at \mathbf{x} uses its 1st subarray to communicate with the typical receiver at \mathbf{y} . By adopting the orthogonality of steering vector, given the transmit steering vector $\mathbf{a}_T(\bar{\theta}_T^{\mathbf{y}\mathbf{x}}, \bar{\phi}_T^{\mathbf{y}\mathbf{x}})$, we have $\mathbf{a}_T(\bar{\theta}_T^{\mathbf{y}\mathbf{x}}, \bar{\phi}_T^{\mathbf{y}\mathbf{x}}) \mathbf{F}_{\text{RF}}^{\mathbf{x}} = \left[\frac{\sqrt{N_T^i}}{N_i}, 0, \dots, 0 \right] \in \mathbb{R}^{1 \times N_i}$ only occurs when the AoD for the typical link is different from that for others served by the transmitter at \mathbf{x} , which has the probability of $\left(1 - \frac{1}{N_T^i}\right)^{N_i - 1}$ for $p_{\text{ZF}}(N_T^i, N_i) = 1$.

Accordingly, we have $\mathbf{f}_{\text{BB},1}^{\mathbf{x}}[k] = \left[\sqrt{\frac{N_i}{N_T^i}}, 0, \dots, 0 \right]^T$ that satisfies $\|\mathbf{F}_{\text{RF}}^{\mathbf{x}} \mathbf{f}_{\text{BB},1}^{\mathbf{x}}[k]\|_F^2 = 1$. Since for large number of antennas, other cases occur with very low probability, i.e., $1 - \left(1 - \frac{1}{N_T^i}\right)^{N_i - 1}$, for tractability, the signal power is approximated to be 0 by setting $p_{\text{ZF}}(N_T^i, N_i) = 0$. Note that $i = m$ denotes the transmitter at the gNB and $i = s$ is that at the IAB-node.

Proposition 1: The beamforming gain (including sidelobe gains) of the inter-cell interference links is given by $p_{\text{BF}}(N_T^i, N_R^j, N_i)$, which can be chosen from one of the values with corresponding probability of occurrence in (11) shown on top of the next page. for $p, q \in \mathbb{N}$, $p + q \leq N_i$, where $N_{T,x}^i$ and $N_{T,y}^i$ ($N_{R,x}^j$ and $N_{R,y}^j$) denotes the number of antennas along x - and y -axis of the transmit (receive) UPA. $g_{T,i}$ and $\hat{g}_{T,i}$ ($g_{R,j}$ and $\hat{g}_{R,j}$) are sidelobe gains at the transmitter (receiver). $i = m, j = s$; $i = s, j = s$; $i = m, j = u$; and $i = s, j = u$ denotes the beamforming gain of the interference from gNBs to the typical IAB-node; IAB-nodes to the typical IAB-node; gNBs to the typical UE; and IAB-nodes to the typical UE, respectively.

Proof: Assume squared UPA, the inner product between transmit steering vectors is $\mathbf{a}_{T,i}^H(\bar{\theta}_1, \bar{\phi}_1) \mathbf{a}_{T,i}(\bar{\theta}_2, \bar{\phi}_2) =$

$$\begin{cases} 1 & \text{if } \bar{\theta}_1 = \bar{\theta}_2, \bar{\phi}_1 = \bar{\phi}_2 \\ g_{T,i} = \frac{1}{\sin^2(0.244) N_{T,x}^i N_{T,y}^i} & \text{if } \bar{\theta}_1 \neq \bar{\theta}_2, \bar{\phi}_1 \neq \bar{\phi}_2 \\ \hat{g}_{T,i} = \frac{1}{\sin(0.244) N_{T,x}^i} & \text{otherwise,} \end{cases} \quad (12)$$

where the sidelobe gains $g_{T,i}$ and $\hat{g}_{T,i}$ are derived according to [4], [29]. Similarly, we can model the inner product between receive steering vectors with sidelobe gains $g_{R,j}$ and $\hat{g}_{R,j}$.

³If X is a Nakagami- M distributed random variable, then $X^2 \sim \text{Gamma}(M, 1/M)$ is a unit mean Gamma distributed random variable.

$$\left\{ \begin{array}{l} p + qg_{T,i}^2 + (N_i - p - q)\hat{g}_{T,i}^2 \\ g_{R,j}^2 [p + qg_{T,i}^2 + (N_i - p - q)\hat{g}_{T,i}^2] \\ \hat{g}_{R,j}^2 [p + qg_{T,i}^2 + (N_i - p - q)\hat{g}_{T,i}^2] \end{array} \right. \begin{array}{l} \text{w.p. } \frac{1}{N_R^j} C_{N_i}^p C_{N_i-p}^q \left(\frac{1}{N_T^i} \right)^p \left(1 - \frac{1}{N_{T,x}^i} - \frac{1}{N_{T,y}^i} + \frac{1}{N_T^i} \right)^q \\ \quad \times \left(\frac{1}{N_{T,x}^i} + \frac{1}{N_{T,y}^i} - \frac{2}{N_T^i} \right)^{N_i-p-q} \\ \text{w.p. } \left(1 - \frac{1}{N_{R,x}^j} - \frac{1}{N_{R,y}^j} + \frac{1}{N_R^j} \right) C_{N_i}^p C_{N_i-p}^q \left(\frac{1}{N_T^i} \right)^p \\ \quad \times \left(1 - \frac{1}{N_{T,x}^i} - \frac{1}{N_{T,y}^i} + \frac{1}{N_T^i} \right)^q \left(\frac{1}{N_{T,x}^i} + \frac{1}{N_{T,y}^i} - \frac{2}{N_T^i} \right)^{N_i-p-q} \\ \text{w.p. } \left(\frac{1}{N_{R,x}^j} + \frac{1}{N_{R,y}^j} - \frac{2}{N_R^j} \right) C_{N_i}^p C_{N_i-p}^q \left(\frac{1}{N_T^i} \right)^p \\ \quad \times \left(1 - \frac{1}{N_{T,x}^i} - \frac{1}{N_{T,y}^i} + \frac{1}{N_T^i} \right)^q \left(\frac{1}{N_{T,x}^i} + \frac{1}{N_{T,y}^i} - \frac{2}{N_T^i} \right)^{N_i-p-q}, \end{array} \quad (11)$$

Recall that the virtual angles are uniformly distributed in their quantization sets, and according to the beamformer design in Section III-B, the proposition can be easily proofed. ■

2) *Access link*: Next, assume the gNB at \mathbf{x}_m uses its u th subarray to communication with the typical UE at $\mathbf{0}$, we derive the SINR expression of the gNB associated typical access link at the subcarrier k , which is cast as $\text{SINR}_{\mathbf{0}\mathbf{x}_m}[k] =$

$$\frac{G_a[k]}{I_{m,a}[k] + I_{s,a}[k] + \mathbb{E} \left\{ \left| (\mathbf{w}_{\text{RF}}^0)^H \mathbf{n}_{a,m}[k] \right|^2 \right\} + \mathbb{E} \left\{ |e_{a,m}[k]|^2 \right\}}, \quad (13a)$$

$$G_a[k] = \frac{P_m}{KN_m} \left| (\mathbf{w}_{\text{RF}}^0)^H \mathbf{H}_{\mathbf{0}\mathbf{x}_m}[k] \mathbf{F}_{\text{RF}}^{\mathbf{x}_m} \mathbf{f}_{\text{BB},u}^{\mathbf{x}_m}[k] \right|^2 \\ \approx \frac{P_m N_T^m (N_R^u)^2 \tilde{h}^{\mathbf{0}\mathbf{x}_m} p_{\text{ZF}}(N_T^m, N_m)}{KN_m^2 R_{\mathbf{x}_m \mathbf{0}}^{\alpha_m}}, \quad (13b)$$

$$I_{m,a}[k] = \frac{P_m}{KN_m} \left\| \sum_{\omega \in \Phi_m \setminus \mathbf{x}_m} (\mathbf{w}_{\text{RF}}^0)^H \mathbf{H}_{\mathbf{0}\omega}[k] \mathbf{F}_{\text{RF}}^{\omega} \mathbf{F}_{\text{BB}}^{\omega}[k] \right\|^2 \\ \approx \sum_{\omega \in \Phi_m \setminus \mathbf{x}_m} \frac{P_m N_T^m (N_R^u)^2 \tilde{h}^{\mathbf{0}\omega} p_{\text{BF}}(N_T^m, N_R^u, N_m)}{KN_m R_{\omega \mathbf{0}}^{\alpha_m}}, \quad (13c)$$

$$I_{s,a}[k] = \sum_{i \in \{L, N\}} I_{s,a}^i[k] \\ = \frac{P_s}{KN_s} \left\| \sum_{i \in \{L, N\}} \sum_{\hat{\omega} \in \Phi_{s,i} \setminus \mathbf{0}} (\mathbf{w}_{\text{RF}}^0)^H \mathbf{H}_{\mathbf{0}\hat{\omega}}[k] \mathbf{F}_{\text{RF}}^{\hat{\omega}} \mathbf{F}_{\text{BB}}^{\hat{\omega}}[k] \right\|^2 \\ \approx \sum_{i \in \{L, N\}} \sum_{\hat{\omega} \in \Phi_{s,i} \setminus \mathbf{0}} \frac{P_s N_T^s (N_R^u)^2 \tilde{h}^{\mathbf{0}\hat{\omega}} p_{\text{BF}}(N_T^s, N_R^u, N_s)}{KN_s R_{\hat{\omega} \mathbf{0}}^{\alpha_{s,i}}}, \quad (13d)$$

where in (13a), $G_{a,m}[k]$, $I_{m,a}[k]$, and $I_{s,a}[k]$ denote the power of the desired signal, that of the interference from non-target gNBs, and that of the interference from IAB-nodes at subcarrier k , respectively; $\mathbb{E} \left\{ \left| (\mathbf{w}_{\text{RF}}^0)^H \mathbf{n}_{a,m}[k] \right|^2 \right\} = \sigma_n^2 N_R^u$ is the Gaussian noise power with $\mathbf{n}_{a,m}[k] \sim \mathcal{CN}(\mathbf{0}, \sigma_n^2 \mathbf{I}_{N_R^u})$; $\mathbb{E} \left\{ |e_{a,m}[k]|^2 \right\}$ represents the ADC quantization noise power with similar definition in (10). In (13b)-(13d), $\tilde{h}^{\mathbf{0}\mathbf{x}_m} = 10^{-0.1(\beta+\chi_m)} |h^{\mathbf{0}\mathbf{x}_m}|^2$, $\tilde{h}^{\mathbf{0}\omega} = 10^{-0.1(\beta+\chi_m)} |h^{\mathbf{0}\omega}|^2$, and $\tilde{h}^{\mathbf{0}\hat{\omega}} = 10^{-0.1(\beta+\chi_{s,i})} |h^{\mathbf{0}\hat{\omega}}|^2$ follow from the composite GL distribution; $p_{\text{ZF}}(N_T^m, N_m)$ is the ZF penalty follows Remark

2; $p_{\text{BF}}(N_T^m, N_R^u, N_m)$ and $p_{\text{BF}}(N_T^s, N_R^u, N_s)$ are beamforming gains follow Proposition 1.

Finally, assume the IAB-node at \mathbf{x}_s^j with $j \in \{L, N\}$ uses its v th subcarrier to provide communications to the typical UE at $\mathbf{0}$, the SINR expression of the IAB-node associated typical access link at the subcarrier k is expressed as $\text{SINR}_{\mathbf{0}\mathbf{x}_s^j}[k] =$

$$\frac{G_{a,s}[k]}{\hat{I}_{m,a}[k] + \hat{I}_{s,a}[k] + \mathbb{E} \left\{ \left| (\mathbf{w}_{\text{RF}}^0)^H \mathbf{n}_{a,s}[k] \right|^2 \right\} + \mathbb{E} \left\{ |e_{a,s}[k]|^2 \right\}} \quad (14a)$$

$$G_{a,s}[k] = \frac{P_s}{KN_s} \left| (\mathbf{w}_{\text{RF}}^0)^H \mathbf{H}_{\mathbf{0}\mathbf{x}_s^j}[k] \mathbf{F}_{\text{RF}}^{\mathbf{x}_s^j} \mathbf{f}_{\text{BB},v}^{\mathbf{x}_s^j} \right|^2 \\ \approx \frac{P_s N_T^s (N_R^u)^2 \tilde{h}^{\mathbf{0}\mathbf{x}_s^j} p_{\text{ZF}}(N_T^s, N_s)}{KN_s^2 R_{\mathbf{x}_s^j \mathbf{0}}^{\alpha_{s,j}}}, \quad (14b)$$

$$\hat{I}_{m,a}[k] = \frac{P_m}{KN_m} \left\| \sum_{\omega \in \Phi_m} (\mathbf{w}_{\text{RF}}^0)^H \mathbf{H}_{\mathbf{0}\omega}[k] \mathbf{F}_{\text{RF}}^{\omega} \mathbf{F}_{\text{BB}}^{\omega} \right\|^2 \\ \approx \sum_{\omega \in \Phi_m} \frac{P_m N_T^m (N_R^u)^2 \tilde{h}^{\mathbf{0}\omega} p_{\text{BF}}(N_T^m, N_R^u, N_m)}{KN_m R_{\omega \mathbf{0}}^{\alpha_m}}, \quad (14c)$$

$$\hat{I}_{s,a}[k] = \sum_{i \in \{L, N\}} \hat{I}_{s,a}^i[k] \\ = \frac{P_s}{KN_s} \left\| \sum_{i \in \{L, N\}} \sum_{\hat{\omega} \in \Phi_{s,i} \setminus \mathbf{x}_s^j} (\mathbf{w}_{\text{RF}}^0)^H \mathbf{H}_{\mathbf{0}\hat{\omega}}[k] \mathbf{F}_{\text{RF}}^{\hat{\omega}} \mathbf{F}_{\text{BB}}^{\hat{\omega}} \right\|^2 \\ \approx \sum_{i \in \{L, N\}} \sum_{\hat{\omega} \in \Phi_{s,i} \setminus \mathbf{x}_s^j} \frac{P_s N_T^s (N_R^u)^2 \tilde{h}^{\mathbf{0}\hat{\omega}} p_{\text{BF}}(N_T^s, N_R^u, N_s)}{KN_s R_{\hat{\omega} \mathbf{0}}^{\alpha_{s,i}}}, \quad (14d)$$

where in (14a), $G_{a,s}[k]$, $\hat{I}_{m,a}[k]$, and $\hat{I}_{s,a}[k]$ denote the power of the desired signal, that of the interference from gNBs, and that of the interference from non-target IAB-nodes at subcarrier k , respectively; $\mathbb{E} \left\{ \left| (\mathbf{w}_{\text{RF}}^0)^H \mathbf{n}_{a,s}[k] \right|^2 \right\} = \sigma_n^2 N_R^u$ is the Gaussian noise power with $\mathbf{n}_{a,s}[k] \sim \mathcal{CN}(\mathbf{0}, \sigma_n^2 \mathbf{I}_{N_R^u})$; $\mathbb{E} \left\{ |e_{a,s}[k]|^2 \right\}$ represents the ADC quantization noise power similar to (10). In (14b)-(14d), $\tilde{h}^{\mathbf{0}\mathbf{x}_s^j} = 10^{-0.1(\beta+\chi_{s,j})} |h^{\mathbf{0}\mathbf{x}_s^j}|^2$, $\tilde{h}^{\mathbf{0}\omega} = 10^{-0.1(\beta+\chi_m)} |h^{\mathbf{0}\omega}|^2$, and $\tilde{h}^{\mathbf{0}\hat{\omega}} = 10^{-0.1(\beta+\chi_{s,i})} |h^{\mathbf{0}\hat{\omega}}|^2$ are composite GL distributed random variables; $p_{\text{ZF}}(N_T^s, N_s)$ is the ZF penalty follows Remark 2; $p_{\text{BF}}(N_T^m, N_R^u, N_m)$ and

$p_{\text{BF}}(N_{\text{T}}^{\text{s}}, N_{\text{R}}^{\text{u}}, N_{\text{s}})$ are beamforming gains follow Proposition 1.

V. PERFORMANCE ANALYSIS

For the standard OFDM system, due to different channel gains occurring on different subcarriers, the effective SINR, whose statistics can be obtained by Log-normal or Gaussian approximations, is used for deriving the performance metrics [30], [31]. However, in this work, thanks to Remark 1, the value of SINR is the same for all subcarriers, resulting in $\text{SINR}[k] \forall k$ equals to the effective SINR. Therefore, $\text{SINR}[k]$ is utilized for analysis and the subcarrier index is omitted for simplicity.

A. Association Probabilities

This subsection introduces the association probabilities, i.e., the probabilities of the typical UE served by a gNB and an IAB-node, based on the maximum *long-term averaged biased-received-desired-signal power* (i.e., $\mathbb{E}\{\text{received-desired-signal power}\} \times \text{bias factor } T_i$, for $i = \text{m}$ if the desired signal comes from the gNB and $i = \text{s}$ if it comes from the IAB-node) criteria [32]. The bias factor plays the role of offloading the traffic from gNB to IAB-node (or from IAB-node to gNB) to satisfy a certain network-wide performance requirement [33]. By tuning the bias ratio $\frac{T_{\text{s}}}{T_{\text{m}}}$, the SINR coverage can be changed, which will be shown in Section VI.

For deriving association probabilities, in following lemmas, we first show the probability density function (PDF) and cumulative distribution function (CDF) of the contact distance (i.e., the distance of a typical point in a point process to its nearest point in an independent point process) for three different cases,

- (i) the typical UE in PPP to its nearest LoS IAB-node in an independent PPP;
- (ii) the typical UE in PPP to its nearest NLoS IAB-node in an independent PPP;
- (iii) the typical UE in PPP to its nearest gNB in an independent MHCPP.

Lemma 1: The CDF of the contact distance from PPP typical UE to PPP LoS/NLoS IAB-node with density $\lambda_{\text{s,L}}(x)/\lambda_{\text{s,N}}(x)$ is cast as

$$F_{R_{\mathbf{x}_s^i \mathbf{o}}}(r_{\text{s},i}) = 1 - e^{-\int_0^{r_{\text{s},i}} 2\pi x \lambda_{\text{s},i}(x) dx}. \quad (15)$$

The corresponding PDF is written as

$$f_{R_{\mathbf{x}_s^i \mathbf{o}}}(r_{\text{s},i}) = 2\pi \lambda_{\text{s},i}(r_{\text{s},i}) e^{-\int_0^{r_{\text{s},i}} 2\pi x \lambda_{\text{s},i}(x) dx}, \quad (16)$$

where $r_{\text{s},i} > 0$ denotes the distance from the PPP typical UE to PPP LoS IAB-node for $i = \text{L}$; and that to PPP NLoS IAB-node for $i = \text{N}$.

Proof: The similar proof can be found in [34]. ■

As for the PDF and CDF of PPP to MHCPP contact distance, it is impossible to give exact expressions due to the correlations among the MHCPP points. Fortunately, the authors in [35] provide a piece-wise model, shown in the

following lemma, which has been verified can provide a very closed solution compared with the empirical data.

Lemma 2: The CDF of the contact distance from PPP typical UE to MHCPP gNB with density λ_{m} and hard-core distance ξ is approximated as $F_{R_{\mathbf{x}_m \mathbf{o}}}(r_{\text{m}}) =$

$$\begin{cases} F_{R_{\mathbf{x}_m \mathbf{o},1}}(r_{\text{m}}) = \pi \lambda_{\text{m}} r_{\text{m}}^2 & 0 \leq r_{\text{m}} \leq \frac{\xi}{2}, \\ F_{R_{\mathbf{x}_m \mathbf{o},2}}(r_{\text{m}}) = 1 - \frac{4 - \pi \lambda_{\text{m}} \xi^2}{4} e^{-\frac{2\pi \lambda_{\text{m}} \xi^2 \left[1 - \left(\frac{2r_{\text{m}}}{\xi}\right)^{\varrho}\right]}{\varrho(4 - \pi \lambda_{\text{m}} \xi^2)}} & r_{\text{m}} > \frac{\xi}{2}. \end{cases} \quad (17)$$

Taking the first derivative with respect to r_{m} , we have the PDF of the contact distance as $f_{R_{\mathbf{x}_m \mathbf{o}}}(r_{\text{m}}) =$

$$\begin{cases} f_{R_{\mathbf{x}_m \mathbf{o},1}}(r_{\text{m}}) = 2\pi \lambda_{\text{m}} r_{\text{m}} & 0 \leq r_{\text{m}} \leq \frac{\xi}{2}, \\ f_{R_{\mathbf{x}_m \mathbf{o},2}}(r_{\text{m}}) = 2\pi \lambda_{\text{m}} r_{\text{m}} \left(\frac{2r_{\text{m}}}{\xi}\right)^{\varrho-2} e^{-\frac{2\pi \lambda_{\text{m}} \xi^2 \left[1 - \left(\frac{2r_{\text{m}}}{\xi}\right)^{\varrho}\right]}{\varrho(4 - \pi \lambda_{\text{m}} \xi^2)}} & r_{\text{m}} > \frac{\xi}{2}, \end{cases} \quad (18)$$

where $r_{\text{m}} > 0$ denotes the distance from the PPP typical UE to MHCPP gNB; $\varrho \approx 0.3686(\lambda_{\text{m}} \pi \xi^2)^2 + 0.0985 \lambda_{\text{m}} \pi \xi^2 + 2$ based on the simulation in [35].

Proof: A detailed proof can be found in [35]. ■

Given the statistics of the contact distance, we now derive probabilities of the typical UE associates to an LoS IAB-node, an NLoS IAB-node, and a gNB, respectively, in the following propositions.

Proposition 2: The probability of the typical UE associates to an LoS/NLoS IAB-node at $\mathbf{x}_s^{\text{L}}/\mathbf{x}_s^{\text{N}}$, denoted as $\mathcal{A}_{\text{s,L}}/\mathcal{A}_{\text{s,N}}$, is cast as

$$\begin{aligned} \mathcal{A}_{\text{s},i} &= \int_0^{\left(\frac{\xi}{2\Delta_{i,1}}\right)^{\frac{\alpha_{\text{m}}}{\alpha_{\text{s},i}}}} \left(1 - F_{R_{\mathbf{x}_m \mathbf{o},1}}\left(r_{\text{s},i}^{\frac{\alpha_{\text{m}}}{\alpha_{\text{s},i}}} \Delta_{i,1}\right)\right) \\ &\times \left(1 - F_{R_{\mathbf{x}_s^j \mathbf{o}}}\left(r_{\text{s},i}^{\frac{\alpha_{\text{s},j}}{\alpha_{\text{s},i}}} \Delta_{i,2}\right)\right) f_{R_{\mathbf{x}_s^i \mathbf{o}}}(r_{\text{s},i}) dr_{\text{s},i} \\ &+ \int_{\left(\frac{\xi}{2\Delta_{i,1}}\right)^{\frac{\alpha_{\text{m}}}{\alpha_{\text{s},i}}} }^{\infty} \left(1 - F_{R_{\mathbf{x}_m \mathbf{o},2}}\left(r_{\text{s},i}^{\frac{\alpha_{\text{m}}}{\alpha_{\text{s},i}}} \Delta_{i,1}\right)\right) \\ &\times \left(1 - F_{R_{\mathbf{x}_s^j \mathbf{o}}}\left(r_{\text{s},i}^{\frac{\alpha_{\text{s},j}}{\alpha_{\text{s},i}}} \Delta_{i,2}\right)\right) f_{R_{\mathbf{x}_s^i \mathbf{o}}}(r_{\text{s},i}) dr_{\text{s},i}, \end{aligned} \quad (19)$$

where $i = \text{L}, j = \text{N}; i = \text{N}, j = \text{L}$. $\Delta_{i,1} = \left(\frac{P_{\text{m}} N_{\text{T}}^{\text{m}} N_{\text{m}}^2 T_{\text{m}}}{P_{\text{s}} N_{\text{T}}^{\text{s}} N_{\text{s}}^2 T_{\text{s}}}\right)^{\frac{1}{\alpha_{\text{m}}}} e^{\frac{(0.1\zeta_{\text{m}} \ln 10)^2 - (0.1\zeta_{\text{s},i} \ln 10)^2}{2\alpha_{\text{m}}}}$ and $\Delta_{i,2} = \frac{(0.1\zeta_{\text{s},j} \ln 10)^2 - (0.1\zeta_{\text{s},i} \ln 10)^2}{2\alpha_{\text{s},j}}$. The integration bound is given by $\frac{\alpha_{\text{s},i}}{\alpha_{\text{s},i}} r_{\text{s},i}^{\frac{\alpha_{\text{m}}}{\alpha_{\text{s},i}}} \Delta_{i,1} = \frac{\xi}{2}$.

Proof: The proof can be found in Appendix-B. ■

Proposition 3: The probability of a typical UE associates to a gNB at \mathbf{x}_m , represented as \mathcal{A}_m , is cast as

$$\begin{aligned} \mathcal{A}_m &= \int_0^{\frac{\xi}{2}} \left(1 - F_{R_{\mathbf{x}_m^{\text{L}} \mathbf{o}}}\left(r_{\text{m}}^{\frac{\alpha_{\text{m}}}{\alpha_{\text{s,L}}}} \Delta_{\text{L}}\right)\right) \\ &\times \left(1 - F_{R_{\mathbf{x}_m^{\text{N}} \mathbf{o}}}\left(r_{\text{m}}^{\frac{\alpha_{\text{m}}}{\alpha_{\text{s,N}}}} \Delta_{\text{N}}\right)\right) f_{R_{\mathbf{x}_m \mathbf{o},1}}(r_{\text{m}}) dr_{\text{m}} \end{aligned}$$

$$\begin{aligned}
& + \int_{\frac{\xi}{2}}^{\infty} \left(1 - F_{R_{\mathbf{x}_s^L} \mathbf{o}} \left(r_m^{\frac{\alpha_m}{\alpha_{s,L}}} \Delta_L \right) \right) \\
& \times \left(1 - F_{R_{\mathbf{x}_s^N} \mathbf{o}} \left(r_m^{\frac{\alpha_m}{\alpha_{s,N}}} \Delta_N \right) \right) f_{R_{\mathbf{x}_m \mathbf{o}, 2}}(r_m) dr_m, \quad (20)
\end{aligned}$$

where $\Delta_i = \left(\frac{P_s N_T^s N_m^2 T_s}{P_m N_T^m N_s^2 T_m} \right)^{\frac{1}{\alpha_{s,i}}} e^{\frac{(0.1\zeta_{s,i} \ln 10)^2 - (0.1\zeta_m \ln 10)^2}{2\alpha_{s,i}}}$ for $i \in \{L, N\}$.

Proof: The proof follows similar steps in Proposition 2 given the condition that the nearest gNB provides higher biased-received-desired-signal power than the nearest LoS and NLoS IAB-nodes. ■

Having obtained the association probabilities, one can get the PDFs of the serving distance (i.e., the distance of the typical UE to its serving gNB or IAB-node) in the following proposition.

Proposition 4: Conditioned on the typical UE is served by its nearest gNB at \mathbf{x}_m , the corresponding PDF of the serving distance is written as

$$\begin{aligned}
\hat{f}_{R_{\mathbf{x}_m \mathbf{o}}}(r_m) &= \frac{1}{\mathcal{A}_m} \left(1 - F_{R_{\mathbf{x}_s^L} \mathbf{o}} \left(r_m^{\frac{\alpha_m}{\alpha_{s,L}}} \Delta_L \right) \right) \\
&\times \left(1 - F_{R_{\mathbf{x}_s^N} \mathbf{o}} \left(r_m^{\frac{\alpha_m}{\alpha_{s,N}}} \Delta_N \right) \right) f_{R_{\mathbf{x}_m \mathbf{o}}}(r_m), \quad (21)
\end{aligned}$$

where $f_{R_{\mathbf{x}_m \mathbf{o}}}(r_m)$ is piece-wise at the point $r_m = \frac{\xi}{2}$ as stated in Lemma 2.

Similarly, conditioned on the typical UE is served by its nearest LoS (or NLoS) IAB-node at \mathbf{x}_s^L (or \mathbf{x}_s^N), the corresponding PDF of the serving distance is given as

$$\begin{aligned}
\hat{f}_{R_{\mathbf{x}_s^i} \mathbf{o}}(r_{s,i}) &= \frac{1}{\mathcal{A}_{s,i}} \left(1 - F_{R_{\mathbf{x}_m \mathbf{o}}} \left(r_{s,i}^{\frac{\alpha_{s,i}}{\alpha_m}} \Delta_{i,1} \right) \right) \\
&\times \left(1 - F_{R_{\mathbf{x}_s^j} \mathbf{o}} \left(r_{s,i}^{\frac{\alpha_{s,i}}{\alpha_{s,j}}} \Delta_{i,2} \right) \right) f_{R_{\mathbf{x}_s^i} \mathbf{o}}(r_{s,i}), \quad (22)
\end{aligned}$$

when $i = L$, we have $j = N$; when $i = N$, we have $j = L$.

According to Lemma 2, $F_{R_{\mathbf{x}_m \mathbf{o}}} \left(r_{s,i}^{\frac{\alpha_{s,i}}{\alpha_m}} \Delta_{i,1} \right)$ is piece-wise at the point $r_{s,i} = \left(\frac{\xi}{2\Delta_{i,1}} \right)^{\frac{\alpha_m}{\alpha_{s,i}}}$ by solving $r_{s,i}^{\frac{\alpha_{s,i}}{\alpha_m}} \Delta_{i,1} = \frac{\xi}{2}$.

Proof: A simple proof can be found in [13, Lemma 4]. ■

In the rest of the subsections, we derive some performance metrics, such as SINR coverage, capacity with outage, and ergodic capacity for the single-hop backhaul mmWave-IBFD/HD-IAB networks. We set the available bandwidth for IBFD communications as W . Assume the HD transmission is in the frequency-division-duplexing (FDD) manner whose available bandwidth is equally divided into two orthogonal portions (i.e., $W/2$), one for the gNB tier and the other for the IAB-node tier.

B. SINR Coverage

We first give the expression on the SINR coverage in the following theorem.

Theorem 1: The SINR coverage of the single-hop backhaul mmWave-IBFD-IAB networks is defined as

$$\begin{aligned}
\mathcal{P}_{\text{FD}}(\tau) &= \mathcal{A}_m \mathbb{P}(\text{SINR}_{\mathbf{o}\mathbf{x}_m} > \tau) \\
&+ \sum_{i \in \{L, N\}} \mathcal{A}_{s,i} \mathbb{P}(\text{SINR}_{\mathbf{o}\mathbf{x}_s^i} > \tau, \text{SINR}_{\mathbf{x}_s^i \mathbf{x}_m} > \tau), \quad (23)
\end{aligned}$$

where τ is the target SINR. $\text{SINR}_{\mathbf{x}_s^i \mathbf{x}_m}$ denotes the backhaul link SINR of the IAB-node at \mathbf{x}_s^i for serving the typical UE. However, solving $\mathbb{P}(\text{SINR}_{\mathbf{o}\mathbf{x}_s^i} > \tau, \text{SINR}_{\mathbf{x}_s^i \mathbf{x}_m} > \tau)$ is intractable. Fortunately, since IAB-nodes and UEs are drawn from homogeneous PPP, according to Slivnyak's theorem, we have [13], [14]

$$\begin{aligned}
\mathbb{P}(\text{SINR}_{\mathbf{o}\mathbf{x}_s^i} > \tau, \text{SINR}_{\mathbf{x}_s^i \mathbf{x}_m} > \tau) &= \mathbb{P}(\text{SINR}_{\mathbf{o}\mathbf{x}_s^i} > \tau) \\
&\times \mathbb{P}(\text{SINR}_{\hat{\mathbf{o}}\mathbf{x}_m} > \tau). \quad (24)
\end{aligned}$$

The solution of this theorem can be found in Appendix-D.

The SINR coverage of the single-hop backhaul mmWave-HD-IAB networks $\mathcal{P}_{\text{HD}}(\tau)$ can be derived similarly to Theorem 1; however, due to FDD, the interference from the other tier and the RSI in the SINR expressions should be removed. Moreover, the Gaussian noise power of HD is reduced by half compared with that of IBFD since the bandwidth of IBFD is twice as large as that of HD.

C. Capacity with Outage

In the following theorem, we derive the expression on the capacity with outage.

Theorem 2: The capacity with outage, i.e., the average rate correctly received over many transmission bursts, of the single-hop backhaul mmWave-IBFD-IAB networks is cast as

$$\mathcal{C}_{\text{FD}}(\tau_{\min}) = W \log_2(1 + \tau_{\min}) \mathcal{P}_{\text{FD}}(\tau_{\min}), \quad (25)$$

where τ_{\min} is a minimum received SINR fixed at the transmitter as the transmitter does not know the instantaneous received SINR, thus should fix a transmission rate independent of that.

Similarly, the capacity with outage of the single-hop backhaul mmWave-HD-IAB networks $\mathcal{C}_{\text{HD}}(\tau_{\min})$ is given by replacing W with $W/2$ and $\mathcal{P}_{\text{FD}}(\tau_{\min})$ with $\mathcal{P}_{\text{HD}}(\tau_{\min})$ in Theorem 2.

D. Ergodic Capacity

The expression on the ergodic capacity is presented in the following theorem.

Theorem 3: The ergodic capacity for the single-hop backhaul mmWave-IBFD-IAB networks, defined as the average of the instantaneous capacity, is written as

$$\mathcal{E}_{\text{FD}} = \mathcal{A}_m \bar{\mathcal{R}}_m + \mathcal{A}_{s,L} \min(\bar{\mathcal{R}}_{s,L}, \bar{\mathcal{R}}_b) + \mathcal{A}_{s,N} \min(\bar{\mathcal{R}}_{s,N}, \bar{\mathcal{R}}_b), \quad (26)$$

where $\bar{\mathcal{R}}_m = \mathbb{E}\{W \log_2(1 + \text{SINR}_{\mathbf{o}\mathbf{x}_m})\}$, $\bar{\mathcal{R}}_{s,L} = \mathbb{E}\{W \log_2(1 + \text{SINR}_{\mathbf{o}\mathbf{x}_s^L})\}$, $\bar{\mathcal{R}}_{s,N} = \mathbb{E}\{W \log_2(1 + \text{SINR}_{\mathbf{o}\mathbf{x}_s^N})\}$ and $\bar{\mathcal{R}}_b = \mathbb{E}\{W \log_2(1 + \text{SINR}_{\hat{\mathbf{o}}\mathbf{x}_m})\}$ represent ergodic capacities of the gNB associated access link, the LoS IAB-node associated access link, the NLoS IAB-node associated access

link, and the backhaul link, respectively, which are derived in Appendix-E.

Likewise, the ergodic capacity of the corresponding HD networks \mathcal{E}_{HD} is given by scaling W in Theorem 3 with $1/2$ and removing the RSI and interference from the other tier in SINR expressions.

Note that we choose the minimum ergodic capacity between the IAB-node associated access link and the backhaul link as the final ergodic capacity at the UE associated with the IAB-node. This is because, in the IAB system, the maximum ergodic capacity that an IAB-node can provide is limited by its corresponding backhaul link [11], [14].

VI. NUMERICAL RESULTS

In this section, we verify theoretical results derived in this paper and evaluate the performance of the single-hop backhaul mmWave-IBFD-IAB networks. Furthermore, for the best understanding of the pros and cons of the IBFD transmission, comparisons are made between IBFD and HD schemes. Unless otherwise specified, the values of simulation parameters are chosen from Table I. Monte Carlo simulations with 10^6 iterations are utilized to verify the accuracy of theoretical results we derived.

A. Association Probabilities and SINR Coverage

Both figures in Fig. 2 show a close match between simulation and analytical results, which indicates a good accuracy given by our approximated analytical results derived in this paper. In Fig. 2(a), we evaluate how the association probabilities can be affected by changing the bias ratio of the IAB-node to the gNB, i.e., $\frac{T_s}{T_m}$. We can find that the association probability of the typical UE associates to an IAB-node, i.e., \mathcal{A}_s , goes up as the ratio increases, and that of the typical UE associates to a gNB, i.e., \mathcal{A}_m , shows an opposite trend since as $\frac{T_s}{T_m}$ increases, more traffic is offloaded from the gNB to the IAB-node.

In Fig. 2(b), we study the impact of $\frac{T_s}{T_m}$ on the SINR coverage. The SINR coverage at a fixed threshold is first increased as $\frac{T_s}{T_m}$ rises, after reaching the maximum at $\frac{T_s}{T_m} = 0$ dB, the SINR coverage reduces as the ratio increases. The reason for decreasing is analyzed as follows. As $\frac{T_s}{T_m}$ increases, \mathcal{A}_s becomes dominant, as shown in Fig. 2(a). Thus, according to Theorem 1, the SINR coverage of the network can be dominated by that of the IAB-node tier from at a high bias ratio. Even if the gNB is tower mounted, which has a direct fiber connection but with limited quantity due to the high deployment cost of fiber connected BSs. Biasing towards wireless IAB-nodes has the potential benefit of reducing the deployment cost. However, since i) the transmit power and propagation properties of the IAB-node are worse than that of the gNB; ii) the performance of the IAB-node associated access link is restricted by the backhaul link; iii) the backhaul link suffers from RSI, the network coverage becomes to distort. Moreover, it is interesting to find that the increase rate of the coverage is much less than the decrement rate.

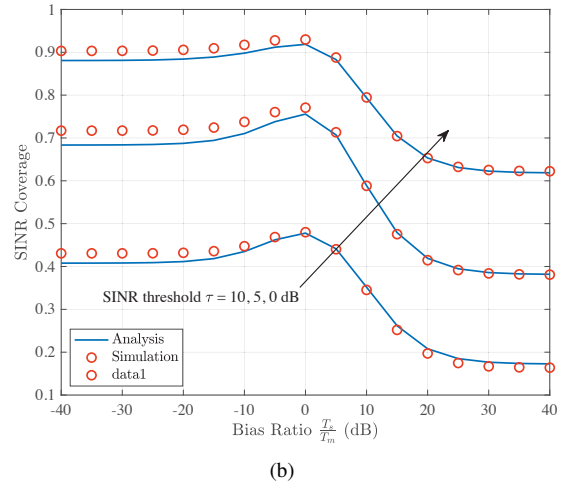
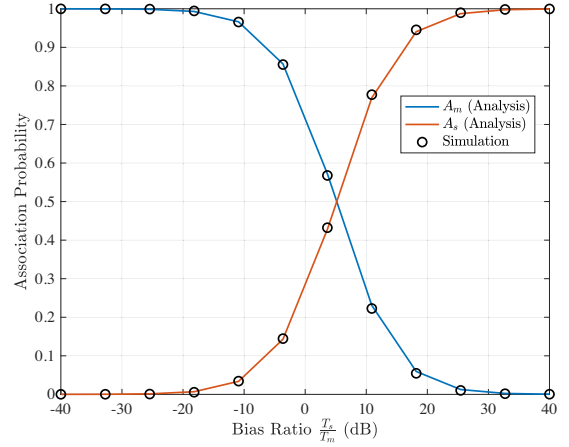


Fig. 2. Verification of theoretical results for (a) association probabilities and (b) SINR coverage v.s. bias ratio $\frac{T_s}{T_m}$ at SINR threshold $\tau = 0, 5, 10$ dB.

B. Capacity with Outage

Assume the transmitter fixes a minimum received SINR at $\tau_{\text{min}} = 0$ dB. In Fig. 3(a), we compare the capacity with outage of single-hop backhaul mmWave-IBFD- and HD-IAB networks in terms of different bias ratios $\frac{T_s}{T_m}$ with various values of RSI controlling factor η . In general, as $\frac{T_s}{T_m}$ increases, the capacity with coverage decreases, which can be explained by Theorem 2 and the analysis in the last subsection. When $\eta > -50$ dB, the effect of RSI on the capacity with outage becomes obvious. However, when $\eta > -20$ dB, the capacity with outage for different values of $\frac{T_s}{T_m}$ tends to be stable. The reason is that high RSI makes the SINR coverage of the IAB-node tier approach to 0; hence, the SINR coverage of the network is nearly dominated by that of the gNB tier. Interestingly, with efficient SIC, for $\frac{T_s}{T_m} = 0$ dB, using IBFD transmission can nearly double the capacity with outage compared with using HD; even if high RSI is reserved, the capacity with outage of IBFD still outperforms that of HD. This is an attractive result since one can benefit from IBFD with high RSI power by tuning $\frac{T_s}{T_m}$ other than exploring difficult and expensive SIC techniques to achieve higher levels of SIC. In addition, the capacity with outage ratio of IBFD to

TABLE I
SYSTEM PARAMETERS AND DEFAULT VALUES

Notation	Physical Meaning	Values
K	Number of subcarriers	512
W	Bandwidth	800 MHz
f_c	Carrier frequency	38 GHz
$M_m, M_{s,L}, M_{s,N}$	Nakagami factor	4, 3, 2
σ_n^2	Gaussian noise power	$-174 \text{ dBm} + 10 \log_{10} W + 10 \text{ dB}$ (IBFD) $-174 \text{ dBm} + 10 \log_{10} \frac{W}{2} + 10 \text{ dB}$ (HD)
ϵ	Blockage density constant	0.0071 [36]
R_0	Radius of analysis region	1000m
ξ	Hard-core distance	100m
$\lambda_m, \lambda_s, \lambda_u$	gNB, IAB-node, and UE density	$1 \times 10^{-5}/\text{m}^2, 4 \times 10^{-5}/\text{m}^2, 2 \times 10^{-4}/\text{m}^2$
η	RSI controlling factor	80 dB
η_{dig}	The amount of digital SIC	25 dB
T	Gamma distribution samples	5 [37]
P_m, P_s	Transmit power	40 dBm, 33 dBm
T_s/T_m	Bias factor ratio	0 dB
N_m, N_s	Number of subarrays	8, 4
N_m^T, N_s^T	Number of transmit antennas	$32 \times 32, 16 \times 16$
N_m^R, N_s^R	Number of receive antennas	$16 \times 16, 8 \times 8$
$\alpha_m, \alpha_{s,L}, \alpha_{s,N}$	Path loss exponent	1.9, 2, 3.3 [38]
$\zeta_m, \zeta_{s,L}, \zeta_{s,N}$	Shadowing effect standard deviation	3.7, 4.3, 10.7 [38]
q	ADC quantization bits	8 bits
$\hat{g}_{T,m}, \hat{g}_{T,s}, \hat{g}_{T,m}, \hat{g}_{T,s}$	Transmitter sidelobe gain	-8.9 dB, -5.9 dB, -17.8 dB, -11.7 dB [4], [29]
$\hat{g}_{R,s}, \hat{g}_{R,u}, \hat{g}_{R,s}, \hat{g}_{R,u}$	Receiver sidelobe gain	-5.9 dB, -2.9 dB, -11.7 dB, -5.7 dB [4], [29]

HD reduces as $\frac{T_s}{T_m}$ increases.

In Fig. 3(b), we also study how the capacity with outage of the single-hop backhaul mmWave-IBFD-IAB network is affected when using ADC with different resolutions in various bias ratios at $\tau_{\min} = 0 \text{ dB}$. It is evident that the capacity with outage can be improved by increasing the ADC quantization bits and reducing the bias ratio. Meanwhile, the capacity with outage saturates when ADC resolution is about higher than 5 bits, indicating that the ADC quantization noise effect becomes negligible compared to other interference and noise in our analyzed network. This result emphasizes the feasibility of using low-resolution ADC in the network. It also should be noted that low-resolution ADCs are preferred in mmWave communications because their low power consumption can compensate for the high power consumption imposed by the numerous RF chains [39].

The simulation results for verifying the analytical results of capacity with outage are omitted since it depends on the SINR coverage, which has been shown a close match between simulation and analytical results in Fig. 2(b).

C. Ergodic Capacity

Fig. 4 compares the network ergodic capacity with varying RSI factor η and hard-core distance ξ between single-hop backhaul FR2-IBFD- and HD-IAB networks in terms of different density ratios of IAB-node to gNB $\frac{\lambda_s}{\lambda_m}$. Fig. 4(a) shows how the RSI affects the network ergodic capacity. Note that when $\frac{\lambda_s}{\lambda_m}$ increases, the effective cell radius of the IAB-node tier reduces, which results in a higher ergodic capacity of the corresponding link. On the contrary, the gNB tier's ergodic capacity reduces due to the UEs are more likely to be served by the IAB-nodes as $\frac{\lambda_s}{\lambda_m}$ increases. When $\eta \leq -50 \text{ dB}$, the IAB-node tier's ergodic capacity increment is higher than the decrement of the gNB tier as the ratio increases. Thus, the overall ergodic capacity increases as the ratio increases. However, for $\eta > -50 \text{ dB}$, the growth of the ergodic capacity of the IAB-node tier is less than the reduction of the gNB tier

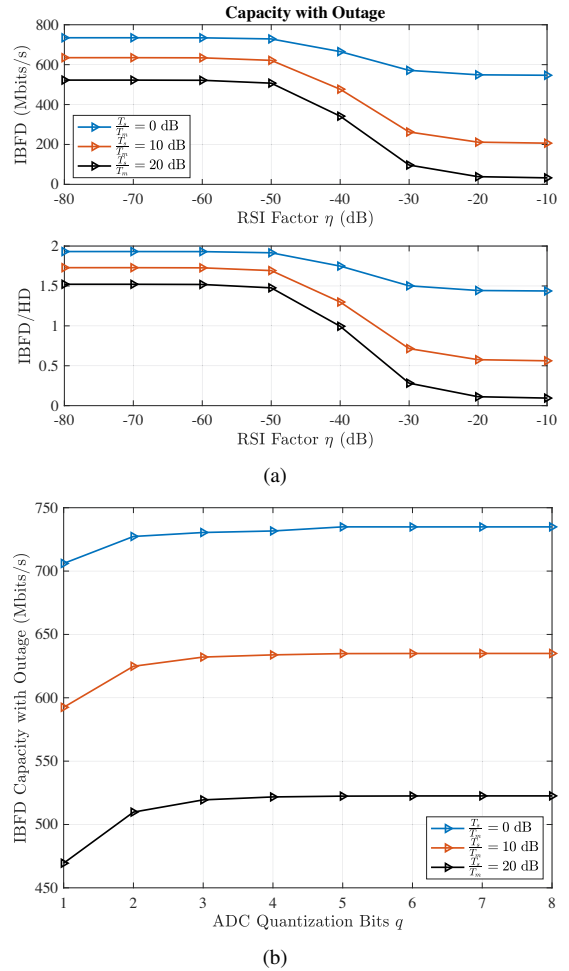


Fig. 3. Single-hop backhaul mmWave-IBFD-IAB networks capacity with outage at a minimum received SINR = 0 dB (i.e., $\tau_{\min} = 0 \text{ dB}$) in terms of $\frac{T_s}{T_m} = 0, 10, 20 \text{ dB}$ (a) v.s. different values of RSI factors; (b) v.s. different values of ADC quantization bits.

as the ratio increases; hence the overall ergodic capacity gives

a decreasing trend as the ratio increases. This result indicates that with successful SIC, the network ergodic capacity can be improved by increasing $\frac{\lambda_s}{\lambda_m}$. Compared with HD transmission, if $\eta \leq -50$ dB, the ergodic capacity given by the IBFD scheme is around 1.6 times higher than that provided by HD transmission, regardless of the density ratio. However, it is obvious that at the high RSI factor η region, the lower the density ratio is, the higher the ergodic capacity is provided by the IBFD, and thus, the higher the ergodic capacity ratio of IBFD to HD $\frac{\mathcal{E}_{IBFD}}{\mathcal{E}_{HD}}$ is. Moreover, a close match between simulation and analytical results is shown in the figure, which indicates a good accuracy given by our analytical results derived for the network ergodic capacity.

In Fig. 4(b), by fixing the density of gNB, the interference given by gNBs is suppressed by increasing the hard-core distance ξ , as ξ increases, the network ergodic capacity is increased, which is the case for both the IBFD and HD schemes. Especially, as ξ increases, the IBFD ergodic capacity gap between different node density ratios is reduced. Interestingly, when ξ is equal to 0, MHCPP converges to PPP, which gives the lowest ergodic capacity. This result highlights the necessities of imposing a suitable distance between gNBs. Moreover, with successful SIC, the IBFD gives higher ergodic capacity than the HD, no matter what ξ is. Simulation results are omitted here since the accuracy of our analytical results on network ergodic capacity has been verified in Fig. 4(a).

VII. CONCLUSION

This paper analyzed the performance of the multi-cell wideband single-hop backhaul mmWave-IBFD-IAB networks using stochastic geometry, where the gNBs are deployed in MHCPP. For the Nakagami- M small fading and the Log-normal shadowing effect, we leveraged the approximated composite GL distribution for network performance analysis. Moreover, the PGFL of PPP was adopted to approximate the mean interference given by gNBs for simplicity. As a result, our closed-form performance metrics showed a close match to simulations. Furthermore, comparisons were made with the performance of the single-hop backhaul mmWave-HD-IAB networks. Numerical results demonstrated that tuning the bias ratio of the IAB-node to gNB the SINR coverage at a fix SINR threshold shows a convex-alike trend. Interestingly, we found that by selecting a suitable bias ratio, the IBFD scheme can always perform better than the HD, even with high RSI power, relaxing the requirement of high-quality SIC techniques. Moreover, at SINR = 0 dB, the effect of ADC quantization noise can be neglected under a lower resolution. As for the network ergodic capacity, fixing the density of gNB, the ergodic capacity was enhanced by deploying gNBs with MHCPP compared to deploying gNBs with PPP, emphasizing the advantage of utilizing MHCPP. Moreover, the larger the hard-core distance, the higher the ergodic capacity. Additionally, with a small RSI power, the ergodic capacity can be improved by increasing the ratio of the density of IAB-node to gNB.

Further work can be focus on finding the transformation properties of the MHCPP, deriving the system performance

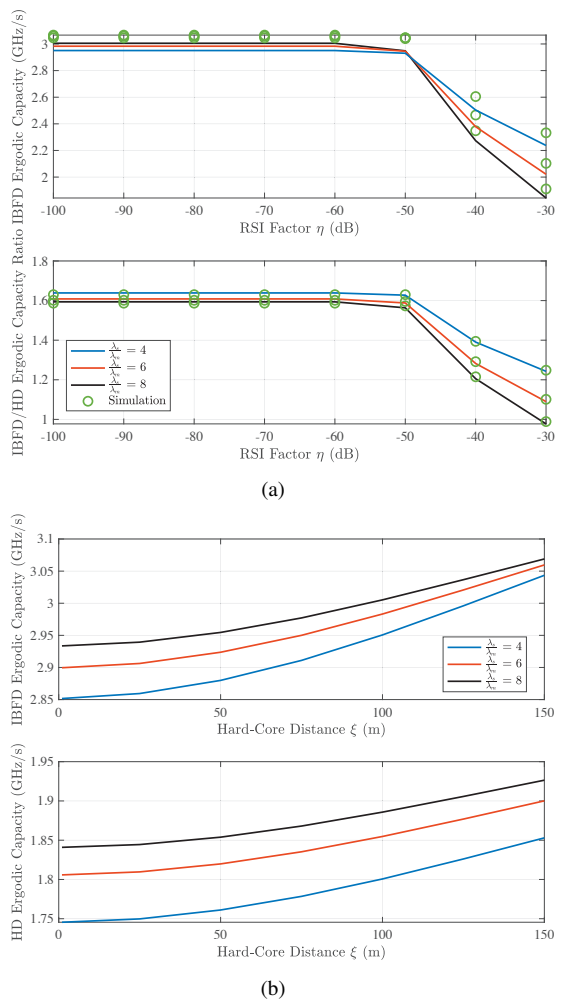


Fig. 4. Single-hop backhaul mmWave-IBFD-IAB networks ergodic capacity in terms of $\frac{\lambda_s}{\lambda_m} = 4, 6, 8$ ($\lambda_m = 1 \times 10^{-5}/\text{m}^2$) (a) v.s. different RSI factor; (b) v.s. different hard-core distance.

with the impact of the hardware impairments and channel estimation error. Moreover, the design and analysis of multi-hop backhaul scenario is worth studying.

APPENDIX A

COMPOSITE GAMMA-LOGNORMAL DISTRIBUTION

Given that $X \sim \text{Gamma}(M, 1/M)$ and $Y \sim \ln\mathcal{N}(\hat{\mu}, \hat{\sigma}^2)$ are independent Gamma and Lognormal distributed random variables, respectively, then $Z = XY \sim \text{GL}(M, \frac{1}{M}, \hat{\mu}, \hat{\sigma}^2)$ is defined as a composite GL distributed random variable with $\mathbb{E}\{Z\} = e^{\hat{\mu} + 0.5\hat{\sigma}^2}$. Since the exact PDF is intractable to derive the corresponding CDF and Laplace transform, a good approximation is provided by [37, Lemma 1].

The corresponding approximated CDF is given as

$$F_Z(z) \approx \frac{1}{\Gamma(M) \sum_{t=1}^T w_t} \sum_{t=1}^T w_t \gamma \left(M, z M e^{-(\sqrt{2}\hat{\sigma}\nu_t + \hat{\mu})} \right), \quad (27)$$

where $\gamma(s, x) = \int_0^x t^{s-1} e^{-t} dt$ is the incomplete gamma function. T , w_t , and ν_t are the number of gamma distribution samples, weight, and abscissas factors for the Gaussian-

Hermite integration, respectively, whose values can be referred from [40].

The Laplace transform is approximated as

$$\mathcal{L}_Z(s) = \mathbb{E} \{ e^{-sz} \} \approx \frac{1}{\sum_{t=1}^T w_t} \sum_{t=1}^T \frac{w_t M^M e^{-M(\sqrt{2}\hat{\sigma}_s \nu_t + \hat{\mu})}}{(s+M e^{-M(\sqrt{2}\hat{\sigma}_s \nu_t + \hat{\mu})})^M}. \quad (28)$$

APPENDIX B

PROOF OF PROPOSITION 2

The typical UE associates to its nearest LoS IAB-node rather than the nearest gNB and NLoS IAB-node, if the nearest LoS IAB-node can provide the highest long-term averaged biased-received-desired-signal power than others, given as

$$\begin{aligned} \mathcal{A}_{s,L} &= \mathbb{P} \left(\frac{P_s N_T^s (N_R^u)^2 T_s}{K N_s^2} \mathbb{E} \{ \tilde{h}^{\mathbf{0}\mathbf{x}_s^L} \} R_{\mathbf{x}_s^L \mathbf{0}}^{-\alpha_{s,L}} \geq \frac{P_m N_T^m (N_R^u)^2 T_m}{K N_m^2} \right. \\ &\quad \times \mathbb{E} \{ \tilde{h}^{\mathbf{0}\mathbf{x}_m} \} R_{\mathbf{x}_m \mathbf{0}}^{-\alpha_m} \cap \frac{P_s N_T^s (N_R^u)^2 T_s}{K N_s^2} \mathbb{E} \{ \tilde{h}^{\mathbf{0}\mathbf{x}_s^L} \} R_{\mathbf{x}_s^L \mathbf{0}}^{-\alpha_{s,L}} \\ &\quad \left. \geq \frac{P_s N_T^s (N_R^u)^2 T_s}{K N_s^2} \mathbb{E} \{ \tilde{h}^{\mathbf{0}\mathbf{x}_s^N} \} R_{\mathbf{x}_s^N \mathbf{0}}^{-\alpha_{s,N}} \right) \\ &\stackrel{(a)}{=} \mathbb{P} \left(\frac{P_s N_T^s (N_R^u)^2 T_s}{K N_s^2} e^{-0.1\beta \ln 10 + \frac{(0.1\zeta_{s,L} \ln 10)^2}{2}} R_{\mathbf{x}_s^L \mathbf{0}}^{-\alpha_{s,L}} \geq R_{\mathbf{x}_m \mathbf{0}}^{-\alpha_m} \right. \\ &\quad \times \frac{P_m N_T^m (N_R^u)^2 T_m}{K N_m^2} e^{-0.1\beta \ln 10 + \frac{(0.1\zeta_{m,L} \ln 10)^2}{2}} \cap \frac{P_s N_T^s (N_R^u)^2 T_s}{K N_s^2} \\ &\quad \times e^{-0.1\beta \ln 10 + \frac{(0.1\zeta_{s,L} \ln 10)^2}{2}} R_{\mathbf{x}_s^L \mathbf{0}}^{-\alpha_{s,L}} \geq \frac{P_s N_T^s (N_R^u)^2 T_s}{K N_s^2} R_{\mathbf{x}_s^N \mathbf{0}}^{-\alpha_{s,N}} \\ &\quad \left. \times e^{-0.1\beta \ln 10 + \frac{(0.1\zeta_{s,N} \ln 10)^2}{2}} \right) \\ &\stackrel{(b)}{=} \int_0^\infty \mathbb{P} \left(R_{\mathbf{x}_m \mathbf{0}} \geq r_{s,L}^{\frac{\alpha_{s,L}}{\alpha_m}} \Delta_{L,1} \right) \mathbb{P} \left(R_{\mathbf{x}_s^N \mathbf{0}} \geq r_{s,L}^{\frac{\alpha_{s,L}}{\alpha_{s,N}}} \Delta_{L,2} \right) \\ &\quad \times f_{R_{\mathbf{x}_s^L \mathbf{0}}}(r_{s,L}) dr_{s,L}, \quad (29) \end{aligned}$$

where (a) is derived by substituting the mean of the power of the composite fading. (b) is given by taking the average on $R_{\mathbf{x}_s^L \mathbf{0}} = r_{s,L}$. By using Lemma 1 and Lemma 2, we can finish the proof. The proof of $\mathcal{A}_{s,N}$ can be given in a similar way.

APPENDIX C

A USEFUL LEMMA

A useful lemma shown below can support the derivation of the SINR coverage. With the following lemma, one can easily deploy the PGFL of PPP to estimate the mean interference from gNBs in the backhaul link and gNB associated access link.

Lemma 3: Given the density of the MHCPP gNB as λ_m with hard-core distance ξ , it can be approximated by thinning the density of its parent PPP $\tilde{\lambda}_m$ with $\rho_M(r_0)$, where $\rho_M(r_0)$ is the conditional thinning Palm probability with $r_0 > 0$ being the distance between two gNBs, which is cast as

$$\rho_M(r_0) = \begin{cases} \frac{2}{\lambda_m(\kappa - \pi\xi^2)} \left[1 - \frac{\pi\xi^2 \tilde{\lambda}_m (1 - e^{-\tilde{\lambda}_m \kappa})}{\tilde{\lambda}_m \kappa (1 - \pi\xi^2 \tilde{\lambda}_m)} \right] & \xi \leq r_0 < 2\xi \\ \rho & r_0 \geq 2\xi \\ 0 & \text{otherwise,} \end{cases} \quad (30)$$

with $\kappa = 2\pi\xi^2 - 2\xi^2 \cos^{-1} \left(\frac{r_0}{2\xi} \right) + r_0 \sqrt{\xi^2 - \frac{r_0^2}{4}}$.

Proof: A proof can be found in [17]. ■

APPENDIX D

SOLUTION OF THEOREM 1

A. Solution of $\mathbb{P}(\text{SINR}_{\mathbf{0}\mathbf{x}_s^L} > \tau)$

The SINR coverage for the LoS IAB-node associated access link is expressed as

$$\begin{aligned} \mathbb{P}(\text{SINR}_{\mathbf{0}\mathbf{x}_s^L} > \tau) &= \left(1 - \frac{1}{N_T^s} \right)^{N_s-1} \int_0^{R_0} \mathbb{P} \left(\tilde{h}^{\mathbf{0}\mathbf{x}_s^L} > \mathcal{G}_s \right. \\ &\quad \left. \times r_{s,L}^{\alpha_{s,L}} \left(\hat{I}_{m,a} + \hat{I}_{s,a}^L + \hat{I}_{s,a}^N + \sigma_n^2 N_R^u \right) \right) \hat{f}_{R_{\mathbf{x}_s^L \mathbf{0}}}(r_{s,L}) dr_{s,L} \\ &\stackrel{(a)}{\approx} \left(1 - \frac{1}{N_T^s} \right)^{N_s-1} \int_0^{R_0} \left[1 - \mathbb{E} \left\{ \frac{1}{\Gamma(M_{s,L}) \sum_{t=1}^T w_t} \sum_{t=1}^T w_t \right. \right. \\ &\quad \left. \left. \times \gamma(M_{s,L}, \mathcal{G}_{s,t}, I) \right\} \right] \hat{f}_{R_{\mathbf{x}_s^L \mathbf{0}}}(r_{s,L}) dr_{s,L} \\ &\stackrel{(b)}{=} \left(1 - \frac{1}{N_T^s} \right)^{N_s-1} \sum_{t=1}^T \sum_{n=0}^{M_{s,L}-1} \frac{w_t}{n! \sum_{t=1}^T w_t} \\ &\quad \times \int_0^{R_0} \mathbb{E} \{ (\mathcal{G}_{s,t} I)^n e^{-\mathcal{G}_{s,t} I} \} \hat{f}_{R_{\mathbf{x}_s^L \mathbf{0}}}(r_{s,L}) dr_{s,L} \\ &= \left(1 - \frac{1}{N_T^s} \right)^{N_s-1} \sum_{t=1}^T \sum_{n=0}^{M_{s,L}-1} \frac{w_t (-\mathcal{G}_{s,t})^n}{n! \sum_{t=1}^T w_t} \frac{d^n}{d\mathcal{G}_{s,t}^n} \\ &\quad \times \left(\int_0^{R_0} \mathbb{E} \{ e^{-\mathcal{G}_{s,t} r_{s,L}^{\alpha_{s,L}} \hat{I}_{s,a}^L} \} \mathbb{E} \{ e^{-\mathcal{G}_{s,t} r_{s,L}^{\alpha_{s,L}} \hat{I}_{s,a}^N} \} \right. \\ &\quad \left. \times \mathbb{E} \{ e^{-\mathcal{G}_{s,t} r_{s,L}^{\alpha_{s,L}} \hat{I}_{m,a}} \} e^{-\mathcal{G}_{s,t} r_{s,L}^{\alpha_{s,L}} \sigma_n^2 N_R^u} \hat{f}_{R_{\mathbf{x}_s^L \mathbf{0}}}(r_{s,L}) dr_{s,L} \right), \quad (31) \end{aligned}$$

where $\mathcal{G}_s = \frac{\tau K N_s^2 \left(1 + \frac{1}{1.5 \cdot 22q} \right)}{P_s N_T^s (N_R^u)^2 \left(1 - \frac{1}{1.5 \cdot 22q} \right)}$, $\mathcal{G}_{s,t} = \mathcal{G}_s M_{s,L} e^{-\nu(\sqrt{2}\hat{\sigma}_s \nu_t + \hat{\mu})}$ with $\hat{\mu} = -0.1\beta \ln 10$ and $\hat{\sigma}_{s,L} = 0.1\zeta_{s,L} \ln 10$. (a) is derived by the approximated CDF of the composite GL distribution and (b) can be referred to [41, eq.(8.4.8)].

Next, we present the mean interference from LoS IAB-nodes in (32) shown on top of the next page, where (c) is derived according to the approximated Laplace transform of the composite GL distribution. After applying the PGFL of PPP, we obtain (d). In (e), we explore the independence on different beamforming gain scenarios, b_i takes one of the beamforming gains from (11), and c_i takes the corresponding probability.

Then, the mean interference from NLoS IAB-nodes $\mathbb{E} \{ e^{-\mathcal{G}_{s,t} r_{s,L}^{\alpha_{s,L}} \hat{I}_{s,a}^N} \}$ can be obtained by the similar step in (32)

with integration from $r_{s,L}^{\frac{\alpha_{s,L}}{\alpha_{s,N}}} \Delta_{L,2}$ to R_0 .

Finally, we derive the mean interference from gNBs. Due to the lack of knowledge on the PGFL of MHCPP, we assume gNBs as a virtual PPP with the density of λ_m to approximate the mean interference, which has been verified can provide a good approximation in [21]. Consequently, with the help of the

$$\begin{aligned}
& \mathbb{E} \left\{ e^{-\mathcal{G}_{s,t} r_{s,L}^{\alpha_{s,L}} \hat{f}_{s,a}^L} \right\} \stackrel{(c)}{\approx} \mathbb{E} \left\{ \prod_{r_{a,L} > r_{s,L}} \frac{1}{\sum_{p=1}^T w_p} \sum_{p=1}^T \frac{w_p M_{s,L}^{M_{s,L}} e^{-M_{s,L}(\sqrt{2}\hat{\sigma}_{s,L}\nu_p + \hat{\mu})}}{\left(\mathcal{G}_{s,t} \frac{P_s N_T^s (N_R^u)^2 r_{s,L}^{\alpha_{s,L}}}{K N_s r_{a,L}^{\alpha_{s,L}}} \text{PBF}(N_T^s, N_R^u, N_s) + M_{s,L} e^{-(\sqrt{2}\hat{\sigma}_{s,L}\nu_p + \hat{\mu})} \right)^{M_{s,L}}} \right\} \\
& \stackrel{(d)}{=} e^{-2\pi \int_{r_{s,L}}^{R_0} \lambda_{s,L}(r_{a,L}) r_{a,L} \left[1 - \frac{1}{\sum_{p=1}^T w_p} \sum_{p=1}^T \frac{w_p M_{s,L}^{M_{s,L}} e^{-M_{s,L}(\sqrt{2}\hat{\sigma}_{s,L}\nu_p + \hat{\mu})}}{\left(\mathcal{G}_{s,t} \frac{P_s N_T^s (N_R^u)^2 r_{s,L}^{\alpha_{s,L}}}{K N_s r_{a,L}^{\alpha_{s,L}}} \text{PBF}(N_T^s, N_R^u, N_s) + M_{s,L} e^{-(\sqrt{2}\hat{\sigma}_{s,L}\nu_p + \hat{\mu})} \right)^{M_{s,L}}} \right] dr_{a,L}} \\
& \stackrel{(e)}{=} \prod_{\substack{i \in \\ \text{PBF}(N_T^s, N_R^u, N_s)}} e^{-2\pi \int_{r_{s,L}}^{R_0} \lambda_{s,L}(r_{a,L}) r_{a,L} \left[1 - \frac{1}{\sum_{p=1}^T w_p} \sum_{p=1}^T \frac{w_p M_{s,L}^{M_{s,L}} e^{-M_{s,L}(\sqrt{2}\hat{\sigma}_{s,L}\nu_p + \hat{\mu})}}{\left(\mathcal{G}_{s,t} \frac{P_s N_T^s (N_R^u)^2 r_{s,L}^{\alpha_{s,L}}}{K N_s r_{a,L}^{\alpha_{s,L}}} b_i + M_{s,L} e^{-(\sqrt{2}\hat{\sigma}_{s,L}\nu_p + \hat{\mu})} \right)^{M_{s,L}}} \right] c_i dr_{a,L}}, \quad (32)
\end{aligned}$$

PGFL of PPP, we have (33) shown on top of the next page, where $\hat{\sigma}_m = 0.1\zeta_m \ln 10$. The solution of $\mathbb{P}(\text{SINR}_{\mathbf{0}_{\mathbf{x}_m^N}} > \tau)$ can be derived in a similarly way.

B. Solution of $\mathbb{P}(\text{SINR}_{\mathbf{0}_{\mathbf{x}_m} > \tau)$

Likewise, the SINR coverage for the typical backhaul link $\mathbb{P}(\text{SINR}_{\mathbf{0}_{\mathbf{x}_m} > \tau)$ can be approximated in a similar way as (31). The mean interference from LoS/NLoS IAB-nodes can be derived from the similar step in (32) with integration limit from 0 to R_0 since the typical IAB-node can only be served by the gNB.

As for the mean interference from other gNBs, we still use the PGFL of PPP to make the approximation, which is given in (34) shown on top of the next page, where $\mathcal{G}_b = \frac{\tau K N_m^2 (1 + \frac{1}{1.5 \cdot 2^{2q}})}{P_m N_T^m (N_R^s)^2 (1 - \frac{1}{1.5 \cdot 2^{2q}})}$, $\mathcal{G}_{b,t} = \mathcal{G}_b M_m e^{-(\sqrt{2}\hat{\sigma}_m \nu_t + \hat{\mu})}$, $r_b = \sqrt{r^2 + r_0^2 - 2rr_0 \cos(\vartheta)}$, $\rho_M(r_0)$ is the thinning probability derived in [17, Lemma 1].

C. Solution of $\mathbb{P}(\text{SINR}_{\mathbf{0}_{\mathbf{x}_m} > \tau)$

Similarly, the SINR coverage for the gNB associated access $\mathbb{P}(\text{SINR}_{\mathbf{0}_{\mathbf{x}_m} > \tau)$ can be approximated follow the step in (31). The mean interference from LoS/NLoS IAB-nodes follows the similar way in (32) with integration limit from $\frac{\alpha_m}{r_m^{\alpha_{s,j}} \Delta_j}$ to R_0 , where $j \in \{L, N\}$. The mean interference from other gNBs can be approximated in a similar way as (34).

APPENDIX E SOLUTION OF THEOREM 3

According to [18, Lemma 2], we have

$$\begin{aligned}
\bar{\mathcal{R}}_m &= \mathbb{E}\{W \log_2(1 + \text{SINR}_{\mathbf{0}_{\mathbf{x}_m})}\} = \left(1 - \frac{1}{N_T^m}\right)^{N_m - 1} \\
&\times \int_0^{R_0} \frac{W}{\ln 2} \int_0^\infty \mathbb{E} \left\{ e^{-z \left(\frac{I_{m,a} + I_{s,a}^L + I_{s,a}^N}{\sigma_n^2 N_R^u} + \frac{1}{(1 + \frac{1}{1.5 \cdot 2^{2q}}) \sigma_n^2 N_R^u} G_{a,m}} \right)} \right\}
\end{aligned}$$

$$\times \left(1 - \mathbb{E} \left\{ e^{-z \frac{G_{a,m}}{(1 + \frac{1}{1.5 \cdot 2^{2q}}) \sigma_n^2 N_R^u}} \right\} \right) \frac{e^{-z}}{z} dz \hat{f}_{R_{\mathbf{x}_m 0}}(r) dr. \quad (35)$$

Like the process in Appendix-D, we can get the solution by leveraging the approximated Laplace transform of the composite GL distribution in (28) and the PGFL of PPP. Similarly, $\bar{\mathcal{R}}_{s,L}$, $\bar{\mathcal{R}}_{s,N}$ and $\bar{\mathcal{R}}_b$ can be easily derived.

REFERENCES

- [1] J. Zhang, N. Garg, M. Holm, and T. Ratnarajah, "Design of full duplex millimeter-wave integrated access and backhaul networks," *IEEE Wireless Commun. Mag.*, vol. 28, no. 1, pp. 60–67, Feb. 2021.
- [2] T. Zhang, S. Biswas, and T. Ratnarajah, "An analysis on wireless edge caching in in-band full-duplex FR2-IAB networks," *IEEE Access*, vol. 8, pp. 164 987–165 002, Sep. 2020.
- [3] S. Park, A. Alkhateeb, and R. W. Heath, "Dynamic subarrays for hybrid precoding in wideband mmWave MIMO systems," *IEEE Trans. Wireless Commun.*, vol. 16, no. 5, pp. 2907–2920, May 2017.
- [4] M. N. Kulkarni, A. Ghosh, and J. G. Andrews, "A comparison of MIMO techniques in downlink millimeter wave cellular networks with hybrid beamforming," *IEEE Trans. Commun.*, vol. 64, no. 5, pp. 1952–1967, March 2016.
- [5] Z. Xiao, P. Xia, and X. Xia, "Full-duplex millimeter-wave communication," *IEEE Wireless Commun. Mag.*, vol. 24, no. 6, pp. 136–143, Dec. 2017.
- [6] H. Luo, A. Bishnu, and T. Ratnarajah, "Design and analysis of in-band full-duplex private 5G networks using FR2 band," *IEEE Access*, vol. 9, pp. 166 886–166 905, Dec. 2021.
- [7] A. Bishnu, M. Holm, and T. Ratnarajah, "Performance evaluation of full-duplex IAB multi-cell and multi-user network for FR2 band," *IEEE Access*, vol. 9, pp. 72 269–72 283, May 2021.
- [8] J. Zhang, H. Luo, N. Garg, A. Bishnu, M. Holm, and T. Ratnarajah, "Design and analysis of wideband in-band-full-duplex FR2-IAB networks," *IEEE Trans. Wireless Commun.*, vol. 21, no. 6, pp. 4183–4196, June 2022.
- [9] 3GPP, "NR; Study on Integrated Access and Backhaul," *TR 38.874 (Rel. 16)*, Dec. 2018.
- [10] J. García-Rois, R. Banirazi, F. J. González-Castaño, B. Lorenzo, and J. C. Burguillo, "Delay-aware optimization framework for proportional flow delay differentiation in millimeter-wave backhaul cellular networks," *IEEE Trans. Commun.*, vol. 66, no. 5, pp. 2037–2051, May 2018.
- [11] C. Saha, M. Afshang, and H. S. Dhillon, "Bandwidth partitioning and downlink analysis in millimeter wave integrated access and backhaul for 5G," *IEEE Trans. Wireless Commun.*, vol. 17, no. 12, pp. 8195–8210, Oct. 2018.

$$\mathbb{E} \left\{ e^{-\mathcal{G}_{s,t} r_{s,L}^{\alpha_{s,L}} \hat{I}_{m,a}} \right\} \approx \prod_{\substack{i \in \\ \mathcal{P}_{\text{BF}}(N_{\text{T}}^{\text{M}}, N_{\text{R}}^{\text{S}}, N_{\text{M}})}} e^{-2\pi \int_{r_{s,L}}^{R_0} \frac{\alpha_{s,L}}{r_{s,L}^{\alpha_{s,L}}} \Delta_{L,1} \lambda_{\text{m}} \left[1 - \frac{1}{\sum_{p=1}^T w_p} \sum_{p=1}^T \frac{w_p M_{\text{m}}^{M_{\text{m}}} e^{-M_{\text{m}}(\sqrt{2}\delta_{\text{m}}\nu_p + \hat{\mu})}}{\left(\mathcal{G}_{s,t} \frac{P_{\text{m}} N_{\text{T}}^{\text{M}} (N_{\text{R}}^{\text{u}})^2 r_{s,L}^{\alpha_{s,L}}}{K N_{\text{m}} r_{\text{a}}^{\alpha_{\text{m}}}} b_i + M_{\text{m}} e^{-(\sqrt{2}\delta_{\text{m}}\nu_p + \hat{\mu})} \right)^{M_{\text{m}}}} \right] c_i r_{\text{a}} dr_{\text{a}}}, \quad (33)$$

$$\mathbb{E} \left\{ e^{-\mathcal{G}_{b,t} r^{\alpha_{\text{m}}} I_{m,b}} \right\} \approx \prod_{\substack{i \in \\ \mathcal{P}_{\text{BF}}(N_{\text{T}}^{\text{M}}, N_{\text{R}}^{\text{S}}, N_{\text{M}})}} e^{-\int_0^{2\pi} \int_{\xi}^{R_0} \tilde{\lambda}_{\text{m}} \rho_{\text{M}}(r_0) \left[1 - \frac{1}{\sum_{p=1}^T w_p} \sum_{p=1}^T \frac{w_p M_{\text{m}}^{M_{\text{m}}} e^{-M_{\text{m}}(\sqrt{2}\delta_{\text{m}}\nu_p + \hat{\mu})}}{\left(\mathcal{G}_{b,t} \frac{P_{\text{m}} N_{\text{T}}^{\text{M}} (N_{\text{R}}^{\text{S}})^2 r^{\alpha_{\text{m}}}}{K N_{\text{m}} r_{\text{b}}^{\alpha_{\text{m}}}} b_i + M_{\text{m}} e^{-(\sqrt{2}\delta_{\text{m}}\nu_p + \hat{\mu})} \right)^{M_{\text{m}}}} \right] c_i r_0 dr_0 d\vartheta}, \quad (34)$$

- [12] M. Polese, M. Giordani, T. Zugno, A. Roy, S. Goyal, D. Castor, and M. Zorzi, "Integrated access and backhaul in 5G mmwave networks: Potential and challenges," *IEEE Commun. Mag.*, vol. 58, no. 3, pp. 62–68, March 2020.
- [13] C. Saha and H. S. Dhillon, "Millimeter wave integrated access and backhaul in 5G: Performance analysis and design insights," *IEEE J. Select. Areas Commun.*, vol. 37, no. 12, pp. 2669–2684, Dec. 2019.
- [14] S. Singh, M. N. Kulkarni, A. Ghosh, and J. G. Andrews, "Tractable model for rate in self-backhauled millimeter wave cellular networks," *IEEE J. Select. Areas Commun.*, vol. 33, no. 10, pp. 2196–2211, May 2015.
- [15] T. S. Rappaport, S. Sun, R. Mayzous, H. Zhao, Y. Azar, K. Wang, G. N. Wong, J. K. Schulz, M. Samimi, and F. Gutierrez, "Millimeter wave mobile communications for 5G cellular: It will work!" *IEEE Access*, vol. 1, pp. 335–349, May 2013.
- [16] S. S. Kalamkar and M. Haenggi, "Simple approximations of the SIR meta distribution in general cellular networks," *IEEE Trans. Commun.*, vol. 67, no. 6, pp. 4393–4406, Feb. 2019.
- [17] J. Lyu and H.-M. Wang, "Secure UAV random networks with minimum safety distance," *IEEE Trans. Veh. Technol.*, vol. 70, no. 3, pp. 2856–2861, March 2021.
- [18] H. He, S. Biswas, P. Aquilina, T. Ratnarajah, and J. Yang, "Performance analysis of multi-cell full-duplex cellular networks," *IEEE Access*, vol. 8, pp. 206914–206930, Nov. 2020.
- [19] H. He, J. Xue, T. Ratnarajah, F. A. Khan, and C. B. Papadias, "Modeling and analysis of cloud radio access networks using Matérn hard-core point processes," *IEEE Trans. Wireless Commun.*, vol. 15, no. 6, pp. 4074–4087, June 2016.
- [20] M. Haenggi, *Stochastic Geometry for Wireless Networks*. Cambridge University Press, 2012.
- [21] —, "Mean interference in hard-core wireless networks," *IEEE Commun. Lett.*, vol. 15, no. 8, pp. 792–794, Aug. 2011.
- [22] T. Bai, R. Vaze, and R. W. Heath, "Analysis of blockage effects on urban cellular networks," *IEEE Trans. Wireless Commun.*, vol. 13, no. 9, pp. 5070–5083, Sep. 2014.
- [23] A. Thornburg, T. Bai, and R. W. Heath, "Performance analysis of outdoor mmWave ad hoc networks," *IEEE Trans. Signal Processing*, vol. 64, no. 15, pp. 4065–4079, Aug. 2016.
- [24] M. Nakagami, "The m-distribution—a general formula of intensity distribution of rapid fading," in *Statistical Methods in Radio Wave Propagation*. W. G. Hoffman, Ed, Oxford, U.K.: Pergamon, 1960.
- [25] A. M. Sayeed, "Deconstructing multi-antenna fading channels," *IEEE Trans. Signal Processing*, vol. 50, no. 10, pp. 2563–2579, Oct. 2002.
- [26] M. N. Kulkarni, A. Alkhatieb, and J. G. Andrews, "A tractable model for per user rate in multiuser millimeter wave cellular networks," in *Proc. 49th Asilomar Conference on Signals, Systems and Computers*, Nov. 2015.
- [27] O. E. Ayach, R. W. Heath, S. Abu-Surra, S. Rajagopal, and Z. Pi, "The capacity optimality of beam steering in large millimeter wave MIMO systems," in *Proc. IEEE SPAWC*, June 2012.
- [28] I. P. Roberts, J. G. Andrews, and S. Vishwanath, "Hybrid beamforming for millimeter wave full-duplex under limited receive dynamic range," *IEEE Trans. Wireless Commun.*, vol. 20, no. 12, pp. 7758–7772, June 2021.
- [29] C. Balanis, *Antenna Theory*. Wiley, 1997.
- [30] R. Giuliano and F. Mazzenga, "Exponential effective SINR approximations for OFDM/OFDMA-based cellular system planning," *IEEE Trans. Wireless Commun.*, vol. 8, no. 9, pp. 4434–4439, Oct. 2009.
- [31] A. Oborina, M. Moisiu, and V. Koivunen, "Performance of mobile MIMO OFDM systems with application to UTRAN LTE downlink," *IEEE Trans. Wireless Commun.*, vol. 11, no. 8, pp. 2696–2706, Aug. 2012.
- [32] H.-S. Jo, Y. J. Sang, P. Xia, and J. G. Andrews, "Heterogeneous cellular networks with flexible cell association: A comprehensive downlink SINR analysis," *IEEE Trans. Wireless Commun.*, vol. 11, no. 10, pp. 3484–3495, Oct. 2012.
- [33] S. Singh, H. S. Dhillon, and J. G. Andrews, "Offloading in heterogeneous networks: Modeling, analysis, and design insights," *IEEE Trans. Wireless Commun.*, vol. 12, no. 5, pp. 2484–2497, May 2013.
- [34] A. Al-Hourani, R. J. Evans, and S. Kandeepan, "Nearest neighbor distance distribution in hard-core point processes," *IEEE Commun. Lett.*, vol. 20, no. 9, pp. 1872–1875, Sep. 2016.
- [35] C. Chen, R. C. Elliott, and W. A. Krzymin, "Empirical distribution of nearest-transmitter distance in wireless networks modeled by Matérn hard core point processes," *IEEE Trans. Veh. Technol.*, vol. 67, no. 2, pp. 1740–1749, Oct. 2018.
- [36] T. Bai and R. W. Heath, "Coverage and rate analysis for millimeter-wave cellular networks," *IEEE Trans. Wireless Commun.*, vol. 14, no. 2, pp. 1100–1114, Oct. 2015.
- [37] K. Cho, J. Lee, and C. G. Kang, "Stochastic geometry-based coverage and rate analysis under Nakagami Log-normal composite fading channel for downlink cellular networks," *IEEE Commun. Lett.*, vol. 21, no. 6, pp. 1437–1440, June 2017.
- [38] A. I. Sulyman, A. T. Nassar, M. K. Samimi, G. R. Maccartney, T. S. Rappaport, and A. Alsanie, "Radio propagation path loss models for 5G cellular networks in the 28 GHz and 38 GHz millimeter-wave bands," *IEEE Commun. Mag.*, vol. 52, no. 9, pp. 78–86, Sep. 2014.
- [39] J. Zhang, L. Dai, X. Li, Y. Liu, and L. Hanzo, "On low-resolution ADCs in practical 5G millimeter-wave massive MIMO systems," *IEEE Commun. Mag.*, vol. 56, no. 7, pp. 205–211, April 2018.
- [40] H. E. Salzer, R. Zucker, and R. Capuano, "Table of the zeros and weight factors of the first 20 hermite polynomials," *Journal of research of the National Bureau of Standards*, vol. 48, pp. 111–116, Feb. 1952.
- [41] F. Olver, D. Lozier, R. Boisvert, and C. Clark, *NIST Handbook of Mathematical Functions*. Cambridge University Press, 2010.